Single-cell sequencing reveals activation of core transcription factors in PRC2-deficient malignant peripheral nerve sheath tumor

Xiyuan Zhang[1], **Hannah E. Lou**[1], **Vishaka Gopalan**[2], **Zhihui Liu**[1], **Hilda M. Jafarah**[1], **Haiyan Lei**[1], **Paige Jones**[1], **Carly M. Sayers**[1], **Marielle E. Yohe**[1], **Prashant Chittiboina**[3], **Brigitte C. Widemann**[1], **Carol J. Thiele**[1], **Michael C. Kelly**[4], **Sridhar Hannenhalli**[2], **Jack F. Shern**[1,5,*]

[1]Pediatric Oncology Branch, Center for Cancer Research, National Cancer Institute, National Institutes of Health, Bethesda, MD 20892, USA

[2]Cancer Data Science Laboratory, Center for Cancer Research, National Cancer Institute, National Institutes of Health, Bethesda, MD 20892, USA

[3]Neurosurgery Unit for Pituitary and Inheritable Diseases, National Institute of Neurological Diseases and Stroke, Bethesda, MD 20892, USA

[4]Center for Cancer Research Single Cell Analysis Facility, Cancer Research Technology Program, Frederick National Laboratory, Bethesda, MD 20892, USA

[5]Lead contact

SUMMARY

Loss-of-function mutations in the polycomb repressive complex 2 (PRC2) occur frequently in malignant peripheral nerve sheath tumor, an aggressive sarcoma that arises from *NF1*-deficient Schwann cells. To define the oncogenic mechanisms underlying PRC2 loss, we use engineered cells that dynamically reassemble a competent PRC2 coupled with single-cell sequencing from clinical samples. We discover a two-pronged oncogenic process: first, PRC2 loss leads to remodeling of the bivalent chromatin and enhancer landscape, causing the upregulation of developmentally regulated transcription factors that enforce a transcriptional circuit serving as the cell's core vulnerability. Second, PRC2 loss reduces type I interferon signaling and antigen presentation as downstream consequences of hyperactivated Ras and its cross talk with STAT/IRF transcription factors. Mapping of the transcriptional program of these PRC2-deficient tumor cells onto a constructed developmental trajectory of normal Schwann cells reveals that changes induced

by PRC2 loss enforce a cellular profile characteristic of a primitive mesenchymal neural crest stem cell.

Graphical Abstract
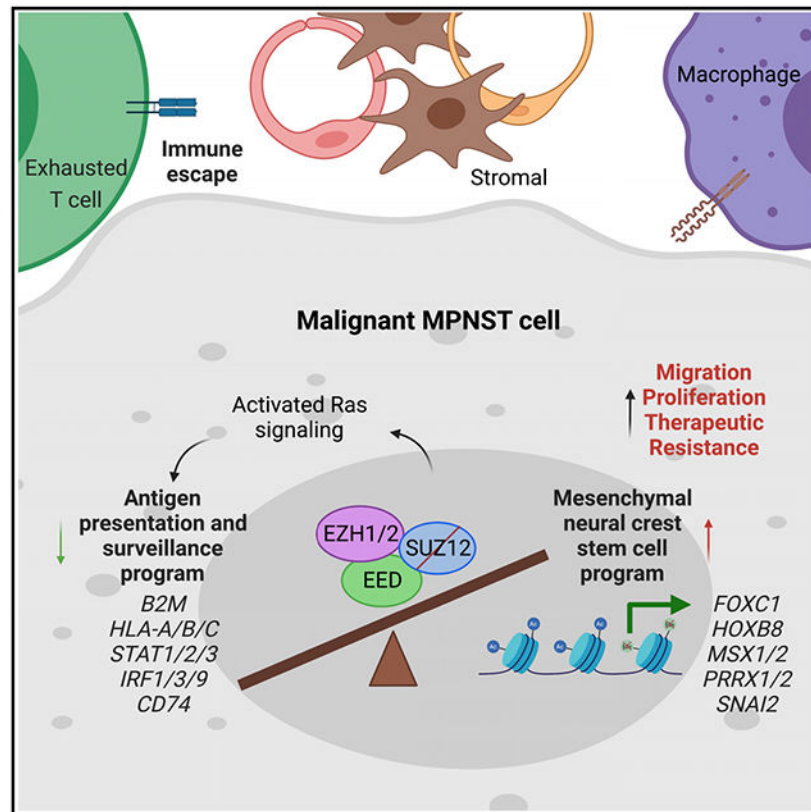
In brief

Zhang et al. provide evidence that PRC2 loss activates cell-fate-determining transcription factors by recruiting active enhancers and dampens type I interferon signaling and antigen presentation through transcriptional cross talk with the hyperactivated Ras. These observations are supported by integrative analysis of single-cell sequencing of patient MPNST samples.

INTRODUCTION

Polycomb repressive complex 2 (PRC2) is a multisubunit histone-modifying (epigenetic) protein complex that catalyzes the trimethylation of histone H3 at lysine 27 (H3K27me3) and is required for proper maintenance of transcriptional repression of key genes during development and cell lineage determination (Bracken et al., 2006; Pasini et al., 2004; Xie et al., 2014). Not surprisingly, given its central role in gene regulation, cancer cells frequently corrupt PRC2 through a variety of mechanisms (Comet et al., 2016; Laugesen et al., 2016). Gain-or loss-of-function alterations of PRC2 in the cancer cell lead to a diversity of downstream consequences such as cellular proliferation (Piunti et al., 2014), invasion (Ren et al., 2012), resistance to apoptosis (Ariës et al., 2018), metastasis (Gupta et al., 2010),

and epithelial-to-mesenchymal transition (Serresi et al., 2016). Interestingly, these tumor cell phenotypes frequently mirror the cellular characteristics observed during normal cellular developmental processes, which raises the intriguing prospect that mutation of PRC2 might enforce the corruption of a primitive cellular program.

Malignant peripheral nerve sheath tumors (MPNSTs) are soft-tissue sarcomas that arise predominantly in patients with neurofibromatosis type 1 (NF1) and follow an aggressive clinical course. Currently, there is no effective medical therapy, and complete surgical removal is required to cure MPNST. Loss of a functional PRC2, through the mutation or deletion of one of its core components *SUZ12* or *EED*, is highly recurrent and present in 60%–90% of all MPNSTs (De Raedt et al., 2014; Lee et al., 2014; Zhang et al., 2014). In MPNST, the loss of PRC2 has a diverse set of consequences, including hyperactivated Ras signaling (De Raedt et al., 2014), increased expression of WNT pathway genes (Lee et al., 2014), and downregulation of genes involved in immune surveillance (Wojcik et al., 2019). In addition, gain of acetylated H3K27 (H3K27ac) accompanying the loss of H3K27me3 has been observed in PRC2-deficient MPNST (De Raedt et al., 2014; Lee et al., 2014; Wojcik et al., 2019). A mechanistic understanding of how the loss of PRC2 results in these diverse, but specific, consequences remains unresolved.

In this study, we sought to improve the basic understanding of PRC2 loss as an oncogenic mechanism in MPNST, and ultimately to define potential therapeutic targets. To accomplish this, we performed a detailed epigenetic and transcriptomic characterization of inducible PRC2 reconstitution cellular systems to discover genomic regions of bivalent chromatin that are dysregulated upon the loss of PRC2. Data from the engineered model systems were integrated with single-cell RNA sequencing (scRNA-seq) and single-cell whole-genome sequencing (scWGS) of PRC2-deficient primary and metastatic human tumors. Through the integration of these datasets, we uncovered that PRC2 loss enforces an immune-suppressive and lineage-specific oncogenic transcriptional program that is characteristic of a neural-crest-derived mesenchymal stem cell.

RESULTS

PRC2 restoration drives a genome-wide gain of H3K27me3 occupation and transcriptional reduction at bivalent domains

To investigate the transcriptomic and epigenetic consequences of PRC2 loss in MPNST, we characterized a panel of human cell lines for their functional PRC2 status based on the presence or absence of H3K27me3 (Figure S1A). Three SUZ12-deficient cell lines were engineered to express a full-length SUZ12 open reading frame (ORF) or an empty vector (EV) under a doxycycline (Dox)-inducible promoter (Figure 1A). These models restored SUZ12 expression in a Dox-dose- and time-dependent fashion (Figures S1A-S1C). Physical reassembly of SUZ12 with EZH2 was validated by immunoprecipitation (Figure S1D), and functional reassembly of the PRC2 complex was confirmed by the induction of H3K27me3 in histone extracts (Figures 1A and S1C).

In PRC2-null T265 cells, PRC2 reconstruction by Dox-induced SUZ12 reexpression inhibited the cell growth in a dose-dependent manner (Figure S1E). Similar dose-dependent

growth-inhibition effects were observed in the other PRC2-null MPNST cell lines as well (Figures S1F and S1G). To profile the transcriptomic consequences of PRC2 loss, we performed RNA-seq in this inducible system. A total of 1,683 and 1,357 genes were significantly downregulated and upregulated, respectively, upon the restoration of a functional PRC2 ($p_{adj} < 0.05$, Table S1). The dominant transcriptional alteration was the downregulation of genes involved in axonogenesis ($p_{adj} = 8.92E–19$), embryonic organs ($p_{adj} = 6.51E–10$), and development regionalization ($p_{adj} = 6.01E–12$) (Figure 1B; Table S1). Strikingly, multiple forkhead (FOX) or homeobox (HOX) transcription factors (TFs) that are critical for cell-fate specification were transcriptionally downregulated by PRC2, including *FOXC1* (log2 fold change [FC] = −1.30, $p_{adj} = 2.81E–05$), *FOXA2* (log2FC = −2.44, $p_{adj} = 1.82E–06$), *HOXB8* (log2FC = −3.11, $p_{adj} = 6.08E–11$), and *PRRX2* (log2FC = −1.29, $p_{adj} = 1.33E–07$). Gene set enrichment analysis (GSEA) demonstrated that genes involved in "Cell_Fate_Commitment" were significantly repressed by PRC2 (enrichment score = −1.98, p = 0; Figure 1C). These results indicated that the loss of PRC2 may contribute to MPNST tumorigenesis via activation of cell-fate-determining TFs.

To characterize the effects of PRC2 restoration on global gain in H3K27me3, we profiled its distribution using chromatin immunoprecipitation with massively parallel DNA sequencing (ChIP-seq) in the inducible cell system. Genome wide, while there was no H3K27me3 signal in PRC2-deficient cells, upon reconstitution of PRC2, we identified 81,549, 48,275, and 33,897 significant H3K27me3 peaks in ST88-14, PT2002, and T265 cells, respectively (Figure 1D). Notably, there were 6,134 peaks common to all three cell lines, and 37,235 peaks were commonly detected in at least two of three cell lines (Figures 1D and 1E). A total of 5,816 genes were associated with these peaks, and interrogation of the RNA-seq for these genes demonstrated that most of these genes were either not expressed (2,923 genes, 50.3%) or transcriptionally unaltered (2,024 genes, 34.8%), regardless of the PRC2 and H3K27me3 status in the cells (Figure 1F). Of the 869 (14.9%) significantly altered genes, 695 (11.9%) were downregulated; and 174 (3%) were upregulated when a functional PRC2 was restored (Figure 1F). ChIP-seq of additional histone marks, including the mutually exclusive mark H3K27ac and bivalent chromatin mark H3K4me3, was also performed. Globally, H3K27ac was reduced in all three cell lines (Figure S1H). The decrease in H3K27ac and unchanged H3K4me3 were notable at sites of H3K27me3 (Figure S1I). Analysis of these sites demonstrated that genes that were both direct PRC2 targets and repressed with the gain of H3K27me3 were significantly enriched at bivalent sites (p < 0.0001; Figure 1G). Bivalent domains marked by both H3K27me3 and H3K4me3 are poised for rapid transcriptional control during development (Bernstein et al., 2006). A total of 850 common bivalent genomic sites were observed in the three cell lines (Figure 1H). Interestingly, the H3K27ac enhancer signal was drastically reduced as the genome regained H3K27me3, and this effect was accompanied by a modest decrease in H3K4me3 signal and chromatin accessibility measured by assay for transposase-accessible chromatin with high-throughput sequencing (ATAC-seq) (Figures 1H, S1J, and S1K).

PRC2-regulated super-enhancer-driven TFs are critical for the survival of MPNST cells

Super enhancers (SEs) are characterized by long stretches of H3K27ac peaks co-occupied by BRD4 and MED; they drive active transcription and are often related to genes specifying

cell identity (Hnisz et al., 2013; Whyte et al., 2013). Consistent with the reduced H3K27ac signals at bivalent domains, the total number of SEs decreased in two of three of our inducible systems as a result of PRC2 restoration (Figure S2A). Since SEs regulate cell-fate-determining TFs that can form a core transcriptional regulatory circuitry and are critical for cancer cell survival (Decaesteker et al., 2018; Durbin et al., 2018; Ran et al., 2018), we next sought to test if PRC2-regulated SE-driven TFs were essential for the survival of MPNST cells. To accomplish this, we identified TFs that were both highly expressed in human MPNST samples and associated with an autoregulated SE (as defined if its own binding motif was identified within its assigned SE) in the three inducible model systems (Figure S2B; Table S2). In total, we compiled a list of 40 MPNST-specific SE-driven TFs that were present in any of the three cell lines (Figure S2C; Table S2) and performed a small interfering RNA (siRNA) screen using a customized library. Three unique siRNAs targeting each candidate gene were selected to ensure coverage across the transcript. Results of the siRNA screen indicated that 17/40 (42.5%) of the TFs were critical for T265 cells (medium growth reduction rate >30%) and 22/40 (55%) of the TFs were essential for ST88-14 cells (Figure 2A; Table S2). Conversely, the knockdown of only one gene (*HOXC4*) in T265 and no genes in ST88-14 increased cell growth by greater than 30% (Table S2). Common essential TFs included *SNAI2*, which demonstrated a 50% growth reduction in five of six cell lines. Interestingly, in the inducible model system, six TFs (*FOXC1*, *HOXB8*, *MSX2*, *FOXD2*, *FOXD1*, and *HOXD13*) demonstrated both loss of H3K27ac and corresponding gain of H3K27me3, indicating that the decreased expression of these TFs was a direct result of PRC2 restoration (Figures 2B and 2C). Two PRC2 direct-target TFs, *FOXC1* and *HOXB8*, were selected for further interrogation because of their association with significant growth reduction in both cell lines. We confirmed the growth rate reduction with individual siRNA-mediated knockdown of these two TFs and observed that the growth rate was dependent on the protein dose for *FOXC1* (Figure 2D) and *HOXB8* (Figure 2E), and this result was true when PRC2 was restored in these cell lines as well as in PRC2 wild-type (WT) cell lines (Figures S2D, S2E, and S2F). CRISPR-Cas9 knockout of *FOXC1* or *HOXB8* in T265 cells resulted in a significant reduction of colony formation when *FOXC1* was knocked out and a trend of decreased colony formation in the *HOXB8* knockdown cells (Figures 2D and 2E). Overall, these results suggest that PRC2-regulated TFs that are derepressed and SE driven as a result of PRC2 loss play a critical role in the survival of MPNST cells.

FOXC1 binds SEs in PRC2-null MPNST cells, enforcing oncogenic signaling

Given the direct PRC2 regulation and significant effect on MPNST cell viability, FOXC1 was selected for further mechanistic characterization. FOXC1 has been reported to bind individual promoters and activate target genes (Shang et al., 2018; Zhu et al., 2017), but its binding has not previously been assessed genome wide. FOXC1-specific ChIP-seq was performed to determine its genome binding in T265, ST88-14, and PT2002 cells with or without the Dox-induced PRC2 restoration. A total of 11,613 peaks (p = 1.0E–05), associated with 4,869 genes, were identified in PRC2-deficient T265 cells (Figures 3A and S3A). PRC2 restoration repressed *FOXC1* transcription (Figures 1B and 2C) and reduced its protein level (Figure 2B), as well as its genome-wide binding signal intensity (Figures 3A and S3C). However, residual FOXC1 in PRC2-restored cells bound the same genomic

loci, albeit with a reduced signal (Figures 3A, S3B, and S3C), and this was highly correlated in all three cell lines (Figure S3D). Among these peaks, only 2.8% (281 peaks) were present at gene promoters (Figures 3A and S3A), and 50.1% (5,821 peaks) of the discovered peaks overlapped with H3K27ac-based active enhancers as defined by Rank Ordering of Super-Enhancers (ROSE) (Lovén et al., 2013; Whyte et al., 2013) (Figures 3A and 3B). Notably, FOXC1 binding at highly expressed genes overlapped with SEs decorated by long stretches of H3K27ac peaks near the gene body (Figures 3C and 3D). PRC2 restoration was noted to reduce FOXC1 binding at these highly expressed genes (Figures S3E and S3F).

To evaluate the regulatory elements associated with FOXC1 binding to the genome, we performed motif analysis of the binding sites and enriched pathway analysis of the associated targeted genes. FOXC1-bound regions were significantly enriched in four classes of motifs: (1) basic region leucine zipper (bZIP) domain-containing TFs, including AP1 family TFs; (2) winged-helix domain-containing FOX TFs; (3) runt homology domain-containing TFs, including RUNX1, RUNX2, and RUNX3; and (4) HOX domain-containing TFs (Figure 3E). Notably, like FOXC1, these TFs were highly expressed in MPNSTs and had a SE associated with the TF gene, and this SE was frequently bound by clusters of FOXC1 peaks, as shown for the *SMAD3* locus (Figure 3C). To further investigate the FOXC1-mediated regulation of these sites, we performed siRNA-mediated FOXC1 knockdown (Figure S3G) and evaluated gene expression and genome levels of H3K27ac by CUT&RUN assay. Knockdown of FOXC1 reduced H3K27ac both globally and at FOXC1 genomic binding sites (Figure S3H). Highlighted genes included *SMAD3*, *TGFBI*, and *RUNX2*, which showed reduction of H3K27ac signals at their identified SE (Figures 3C, 3D, and S3I). Interestingly, FOXC1 knockdown increased *SMAD3* (Figure 3C) and *RUNX2* (Figure S3I) expression while decreasing *TGFBI* (Figure 3D), indicating the potential for complex control of FOXC1 target genes. Interrogation of the motifs of these genes' H3K27ac peaks predicted that they bound one another's SE (Figures S3J and S3K). Therefore, we hypothesized that FOXC1, induced by PRC2 loss, plays a critical role in MPNST oncogenesis by participating in a core TF regulatory circuit (Assi et al., 2019; Somerville et al., 2015). Gene ontology (GO) pathway enrichment analysis of the FOXC1-bound enhancer-associated genes revealed neuron development and differentiation, extracellular matrix formation, and Ras signaling (Figure 3F; Table S3). RNA-seq of CRISPR-Cas9 knockout of *FOXC1* identified that 45% (195/436) of the downregulated and 24% (92/377) of the upregulated genes had corresponding FOXC1 ChIP-seq peaks (Figure 3G). Down-regulation of the Ras signaling gene set, which has previously been described as a feature of PRC2 restoration (De Raedt et al., 2014), was also significantly downregulated with *FOXC1* knockout (enrichment score −0.34, p = 0.037; Figure 3H). In summary, these findings indicated that FOXC1 participates in a core transcriptional regulatory circuit at SEs of highly expressed genes and drives MPNST oncogenesis by regulating critical pathways, including Ras (Figure S3L).

PRC2 restoration indirectly upregulates interferon signaling and antigen presentation

Consistent with its known repressive role, PRC2 restoration resulted in the dominant downregulation of aberrantly activated genes (Figure 1). However, 1,357 genes were significantly upregulated ($p_{adj} < 0.05$) when PRC2 was restored. Pathway enrichment

analysis demonstrated that upregulated genes were involved in type I interferon signaling (p_{adj} = 1.0E–06) and extracellular matrix organization (p_{adj} = 5.6E–10) (Figure 4A; Table S1). Consistent with the repressive function of PRC2, only 177 (13%) of the upregulated genes exhibited a corresponding gain of H3K27me3 signal, while 718 (43%) of the downregulated genes gained a H3K27me3 mark in the Dox-treated cells (p < 0.0001, Figure 4B). The 174 PRC2-targeted upregulated genes were not found to be enriched at bivalent regions compared with the other PRC2-targeted genes (16.1% versus 38.4%, p < 0.0001; Figure 4C). Taken together, these results indicated that the upregulation of genes involved in the type I interferon signaling and extracellular matrix organization occurred as an indirect effect of PRC2 restoration.

The downregulation of proteins involved in type I interferon signaling and antigen presentation has been reported in PRC2-null MPNSTs at the protein level compared with MPNSTs that retain PRC2 (Wojcik et al., 2019). Notably, the upregulated genes in our inducible model system mirrored this observation at the RNA level for these two processes (Figures 4D and 4E). We further confirmed the transcriptional observations at the protein level and found the induction of HLA-A, -B, and -C on the cell surface of PRC2-restored MPNST cells (Figures S4A and S4B), as well as an increase in multiple type I interferon signaling proteins (Figure S4C). To understand the apparent indirect mechanism underlying the induction of these genes, we analyzed 4,824 H3K27ac peaks associated with the upregulated genes in T265 cells (Figure S4D). The signal intensity of these H3K27ac peaks was significantly higher in the Dox-treated sample (Figure S4E), indicating the possible transcriptional regulation of these genes through recruitment of the transcriptional machinery to these regions. Motif profiling of these H3K27ac peaks demonstrated the presence of AP1 family TFs and, interestingly, an enrichment for the IRF family TFs as potential regulators (Figure S4F).

Hyperactive Ras has previously been shown to downregulate immune signaling (Gimple and Wang, 2019), so we hypothesized that this same mechanism might explain our observations. Indeed, in the inducible system, we observed the downregulation of the Ras signaling gene set as a direct consequence of PRC2 restoration (Figure 4F). Interestingly, upon PRC2 restoration, we observed the upregulation of several STAT and IRF family TFs (Figures 4G and S4C), which are responsible for the transcriptional activation of the downstream interferon genes. In addition, inhibition of Ras signaling by MEK inhibitors (MEKis) has previously been shown to induce STAT signaling (Franklin et al., 2020), and phosphorylated ERK2 can act as a TF whose transcriptional activity can be modulated by MEKis (Tee et al., 2014; Yohe et al., 2018). To test this, we treated T265 cells with the MEKi trametinib, and assessed the induction of these immune-modulatory TFs. Importantly, treatment with the MEKi recapitulated the upregulation of multiple STAT and IRF family members (Figure 4H). Finally, treatment of three PRC2-deficient cell lines with a MEKi resulted in the upregulation of HLA-A, -B, and -C on the cell surface (Figure 4I). In summary, PRC2 restoration caused upregulation of immune genes, and this effect was mediated by inhibition of Ras signaling (Figure S4G).

Single-cell sequencing of PRC2-deficient MPNSTs reveals the cellular heterogeneity within primary and metastatic MPNSTs

By restoring PRC2 in MPNST cells, we identified the aberrant activation of SE-driven TFs and inactivation of immune-related genes caused by the loss of PRC2 in MPNST cells. To correlate the results obtained in cell culture systems with primary human tumors, we performed scRNA-seq on a PRC2-deficient, high-grade MPNST that was sampled at multiple time points through the patient's clinical course (diagnostic needle biopsy, resection of the primary tumor, and resection of a metastatic lung tumor; Figure 5A). After quality control, scRNA-seq data for 56,272 cells were available for downstream analysis, including 20,469 cells from the primary MPNST (9,642 and 10,827 cells from the core needle biopsy and primary resection, respectively) and 35,803 from the metastatic resection. Based on the transcription profile, the cells were separated into 18 distinct clusters (Figure 5B), which were annotated based on the expression of canonical markers (Table S4). These clusters broadly included tumor cells, stromal cells, and immune cells (Figure 5C). There was a notable increase in the tumor cell compartment and contraction of the stromal and immune compartments in the metastatic lesion compared with the primary lesion (Figure 5C and Table S4).

To ensure the accurate identification of the malignant cells within the heterogeneous tumor, copy number variation (CNV) was profiled using single-cell whole-genome profiling (scCNV) in 1,270 cells from the primary tumor. Clustering of the cells based on CNV profiles demonstrated a subgroup of 226 cells that were distinct (Figure S5A). Given that the patient had a known germline microdeletion at the *NF1* locus, all cells in the primary MPNST exhibited loss of one allele around the *NF1* gene, while a subgroup of cells demonstrated loss of both alleles (Figure S5B). To link scCNV-profiled cells with scRNA-seq profiling, we inferred copy number changes using the scRNA-seq data compared with the immune component of this dataset (Figure S5C). The MPNST cells profiled for scCNV matched precisely with the CNV pattern predicted by the scRNA-seq, indicating proper classification of the malignant cells. Gain of chromosome 8, which has been proposed as an early or founding genomic change in MPNST (Dehner et al., 2021), was a common unique feature of the identified tumor cells (Figure S5D), and was identified by both scRNA-seq and scCNV.

Using the scRNA-seq data, we derived marker genes that defined each distinct cell cluster (Figures S6A and S6B; Table S4) within the primary and metastatic MPNSTs. Oncogenic pathway and hallmark gene set enrichment of the marker genes in the malignant cells revealed key oncogenic processes and, strikingly, pathways involved in the epithelial-mesenchymal transition and maintenance of embryonic stem cells (Figure 5D and S6C). Genes involved in these pathways included target genes of FOXC1, such as *PRRX1*, *WIF1*, and *TGFBI*, that play critical roles during fate commitment of stem cells (Soldatov et al., 2019). This observation validated our findings from the inducible model systems that PRC2 loss activates FOXC1 and other key TFs in MPNST cells.

The large number of cells in the tumor cell compartment of the metastatic MPNST allowed us to identify distinct tumor subclusters within that lesion. These subclusters were present in the primary tumor, albeit at lower numbers (Figures 5E and 5F). One subcluster of cells

(cluster 7) that dominated the primary tumor was markedly diminished in the metastatic tumor (64.2% versus 0.5% of malignant cells in the primary versus the metastatic MPNST, respectively; Figures 5E and 5F). Interestingly, the marker genes that characterized this cluster were the immune genes, including IFN and antigen presentation genes, that we identified as indirectly upregulated by PRC2 in our inducible cell line system (Figure S6D). By comparing the expression levels of these genes between the primary and the metastatic tumors, we discovered that these genes were significantly more highly expressed in the primary MPNST (Figure S6E). Interestingly, FOXC1 and Ras expression profiles were noted to be expressed universally, with notable increases in the cells taken from the metastatic lesion (Figures 5G and 5H). Overall, our analysis of scCNV and scRNA-seq of the paired primary and metastatic MPNSTs correlated with the model system findings that PRC2 loss maintains a stem-like oncogenic transcriptional program in the malignant cells and simultaneously diminishes immune presentation of the tumor cell.

Malignant cells in MPNSTs map to a dedifferentiated phenotype

Loss of PRC2 in MPNST results in an upregulation of stem cell signature genes in both the cell model systems and patient tumors, and PRC2 restoration in the PRC2-deficient cells reversed this process. Given these results and the known functions of PRC2 in normal Schwann cell (SC) development (Ma et al., 2015, 2016, 2018), we hypothesized that the MPNST cell might be harnessing a distinct developmental transcription program along the SC trajectory. To evaluate this hypothesis, we used single-cell transcriptomic profiling of mouse tissues (Furlan et al., 2017; Soldatov et al., 2019; Wolbert et al., 2020) at each SC developmental stage (E8.5, E12.5/E13.5, mature) to build a normal SC developmental trajectory. We merged single-cell transcriptomes of normal SCs and their precursors from three individual scRNA-seq studies and computationally integrated them to build a developmental trajectory (Figure 6A). As expected, uniform manifold approximation and projection for dimension reduction (UMAP) clustering identified each subtype of the SC lineage moving from neural crest stem cell (NCSC) to SC precursor (SCP) and branching into the transcriptionally distinct nonmyelinating SC (nmSC) and myelinating SC (mySC). The integrated analysis of these cells depicted a developing SC trajectory with the pseudotimes matching the known chronological development order (Mirsky and Jessen, 1996; Mirsky et al., 1996) (Figure 6B). Highly expressed TFs are the key drivers of this lineage during development and are responsible for cell-fate determination (Hnisz et al., 2013; Saint-André et al., 2016; Whyte et al., 2013). Therefore, we derived marker genes of each cell type based on differential expression analysis and used SCENIC (Aibar et al., 2017) to infer the key TFs characteristic of each developmental stage. Marker genes of each cell type accurately distinguished among cell types (Figure S7A; Table S5). In addition, critical TFs known to distinguish particular cell subtypes were correctly placed on the developmental trajectory (Figure 6C), such as the expression of EGR2 and AP1 family TFs (e.g., FOS, JUNB) in the mySC (Stolt and Wegner, 2016). Strikingly, the previously identified PRC2-regulated SE-driven TFs, PRRX1/2 and FOXC1, were among the unique identifiers of the mesenchyme NCSC. Therefore, we hypothesized that the PRC2-deficient MPNST cell was harnessing transcriptional circuits of the mesenchyme NCSC. To test this hypothesis in an unbiased way, we used AUCell (Aibar et al., 2017) to compute the expression of marker genes, derived from cells in the normal SC developmental trajectory,

in malignant cells and normal SCs identified in the human MPNST scRNA-seq data. As predicted, normal SCs from the primary MPNST exhibited the highest similarity to mature mySC, followed by nmSC (Figure 6D; Table S5). Malignant MPNST cells highly expressed marker genes of nmSC but showed lower expression of marker genes of mySC while also upregulating the expression of marker genes characteristic of mesenchyme NCSC (p < 0.0001) and early migratory cells (Figure 6D). Overall, these results suggest that malignant MPNST cells activated a transcriptional program that is characteristic of the mesenchyme NCSC along the normal SC developmental trajectory.

PRC2-regulated TFs establish and reinforce the oncogenic program of MPNST

Next, we compared the transcriptional programs of the malignant cells (27,796 cells from primary and metastasized MPNSTs) with the benign SCs (161 cells from the primary MPNST) of the MPNST and identified genes that were uniquely expressed in the malignant cells (838 genes) and benign SCs (1,493 genes, Table S6). The transcriptomic differences established by these two groups of marker genes could distinctly separate the benign cells from the malignant cells (Figure 7A). Next, we compared these genes with the differentially expressed genes in our PRC2 inducible MPNST cell lines (Figure 1A) and CRISPR-Cas9 FOXC1 or HOXB8 knockout cells (Figures 2C and 2D). Genes downregulated by PRC2 restoration or FOXC1 or HOXB8 loss were significantly enriched among the markers of malignant cells, while genes upregulated by these manipulations were enriched among the SC markers (Figure 7B). The average expression levels of TFs that were downregulated with PRC2 restoration (155 TFs, Table S6) were distinctly highly expressed in the malignant cells (Figure 7C, left). In addition, the directly PRC2-targeted TFs (81 TFs, Table S6) distinguished the malignant cells from all other cells within the patient MPNST (Figure 7C, right). Indeed, the expression levels of SE-driven TFs (40 TFs shown in Figure 2A) were significantly higher compared with other TFs (Figure 7D), indicating that the transcriptional network formed by these highly expressed, SE-driven TFs participates in the oncogenic program that drives the human MPNST. To validate these findings in a broader panel of tumors, we interrogated *FOXC1*, all PRC2-downregulated TFs, and directly PRC2-targeted TFs in a panel of eight low-passage MPNST patient-derived xenograft models (Figures S7B, S7C, and S7D). These PRC2-regulated TFs were universally expressed by MPNST cells.

To refine the discovered TF circuit, motif analysis was performed to identify potential transcriptional regulators of the malignant marker genes in MPNST. First, we scanned the promoters and enhancers near these genes as defined by the H3K27ac peaks in the inducible MPNST cell lines. This analysis demonstrated that known motifs of the SE-driven TFs were positively enriched in the identified promoters (Figure 7E, left) and enhancers (Figure 7E, right). Strikingly, FOXC1 binding sites were overrepresented in promoters and enhancers of malignant marker genes (Figure 7E). Motifs for TFs directly regulated by FOXC1 (Figure 3F), such as *GLI3*, *TWIST1*, and *PRRX1/2*, were also positively enriched in the promoters and enhancers of these marker genes. The high expression of these FOXC1 directly regulated genes was unique to the malignant cells of the patient MPNST sample and these genes were not found to be expressed in the benign SCs (Figures S7E). To confirm this observation in an independent patient, we performed scRNA-seq from a second PRC2-deficient human MPNST and performed clustering analysis (Figure 7F). Again,

FOXC1 was highly expressed and uniquely defined the malignant cells of this patient's tumor (Figure 7G). Mirroring our previous observations, the average expression levels of the defined SE-driven TFs were again significantly higher compared with the other TFs (Figure 7H). Finally, results of the motif enrichment analysis showed that the FOXC1 motif was significantly positively enriched in the enhancers of the marker genes of the malignant cells of this tumor (Figure 7I), indicating its potential function in sustaining the oncogenic program of MPNST. Overall, these results suggest that PRC2 loss and subsequent activation of FOXC1 serves a critical transcriptional regulatory role in driving the oncogenic program of human MPNST.

DISCUSSION

Loss or dysregulation of functional PRC2 is a common oncogenic lesion in human cancer (Comet et al., 2016), and deletions in PRC2 have been shown to be enriched in chemotherapy-resistant Ras mutant tumors (Guerra et al., 2020). Combining inducible models of PRC2 reconstitution and single-cell profiles from clinical specimens, we provide mechanistic details of how the genetic loss of PRC2 activates developmentally specific TFs and enforces stem-like properties in the MPNST cell while dampening the immune presentation of the cell. Specifically, our studies revealed that loss of PRC2 results in direct loss of H3K27me3 and gain of H2K27ac at bivalent, developmentally regulated genes, including *FOXC1* and *HOXB8*. Mechanistically, these changes activate a gene program characteristic of a mesenchymal stem cell and concurrently suppress Ras-mediated, STAT/IRF-driven programs that are critical for immune surveillance. These findings have important implications for how future therapeutic strategies might be employed to target these highly refractory tumors.

Our study defined a group of core TFs, including FOXC1 and HOXB8, that are upregulated as a result of loss of H3K27me3 and gain of H3K27ac in the MPNST cell. Enhancers marked by extensive stretches of H3K27ac determine cell fate and identity by driving the expression of master TFs (Whyte et al., 2013). Multiple studies of diverse cancer subtypes have demonstrated the critical role that these cell-type-specific SEs and TFs play in tumorigenesis (Decaesteker et al., 2018; Durbin et al., 2018; Ran et al., 2018). Our work nominated FOXC1 as a PRC2-dependent switch that is activated in the malignant transformation of the MPNST cell. FOXC1 is known to activate transcription of downstream targets (Hannenhalli and Kaestner, 2009; Jackson et al., 2010; Pierrou et al., 1994) and has previously been shown to regulate proliferation and the epithelial-to-mesenchymal transition that defines a clinically aggressive subtype of breast cancer (Ray et al., 2010; Taube et al., 2010). Interestingly, in acute myeloid leukemias (AMLs), 20% of tumors have FOXC1 overexpression due to regional loss of H3K27me3 at the FOXC1 promoter, which is correlated with co-existing overexpression of members of the HOX TF family (Somerville et al., 2015), mirroring our observations in MPNST. In addition to PRC2-mediated regulation, transcription of FOXC1 is induced by activated mitogen-activated protein kinase (MAPK) signaling (Cauchy et al., 2015). In this context, FOXC1 activates an abnormal regulatory network defined by its downstream target genes (Assi et al., 2019). The potential interplay of FOXC1 with hyperactivated Ras signaling is further evidenced by the presence of an ERK dependent phosphorylation of FOXC1 that improves its protein stability and transcriptional

activities (Berry et al., 2006). Further mechanistic understanding of the cross talk between Ras signaling and FOXC1 in the context of the NF1-deficient MPNST cell could further define FOXC1's role as a central transcriptional node in Ras-driven malignancies. While TFs remain in the "undruggable" category, the improvement of small-molecule targeting of transcription (Struntz et al., 2019) and the development of proteolysis targeting chimeric (PROTAC) technology (Bushweller, 2019) provide future potential therapeutic avenues to target these vulnerabilities in MPNST.

Our findings highlight that the MPNST cell transcriptional program mirrors gene programs characteristic of neural-crest-derived mesenchymal cells. SCs from the dorsal root ganglia are known as the cell of origin of NF1-associated plexiform neurofibromas (PNFs) (Chen et al., 2014) and these neoplastic $NF1^{-/-}$ SCs undergo malignant transformation with the loss of $CDKN2A$ and PRC2 to give rise to MPNSTs (Kim et al., 2017; Zhang et al., 2020). Our analysis discovered that the MPNST cell accomplishes this by corrupting the SC-specific transcriptional regulatory network pioneered by stage-specific TFs (Ma et al., 2018; Stolt and Wegner, 2016) that are driven by H3K27ac-marked enhancers (Ghislain and Charnay, 2006; Jagalur et al., 2011; Reiprich et al., 2010). Our integrated scRNA-seq analysis enabled us to compare the MPNST cell across the entire trajectory of normal SC development. Our observation that MPNST cells transcriptionally mirror mesenchymal cells is consistent with the observation of stem-cell-like features of MPNST reported by others (Spyra et al., 2011; Sun et al., 2021). In addition, it is interesting to note FOXC1's role in development and neural crest specification (Rice et al., 2003; Sun et al., 2013; Tribulo et al., 2003). Indeed, FOXC1 is transiently expressed in the mesenchymal NCSCs during the early phase of SC development and thereafter is properly repressed by PRC2-mediated H3K27me3 as the cells commits to an SC lineage (Soldatov et al., 2019). The understanding of MPNST in the context of embryonic development is reminiscent of other tumors of neural crest origin, such as neuroblastoma (Dong et al., 2020; Jansky et al., 2021; Kameneva et al., 2021). Future efforts could be designed to epigenetically drive the MPNST cell toward a more differentiated phenotype that would eliminate the self-renewal capacity and migratory nature of these cells (de Thé, 2018).

Finally, the incorporation of single-cell sequencing of clinical samples allowed us to interrogate the cancer cell-immune cell cross talk in MPNSTs. Our results align well with the reports from elegant proteomic studies that found decreased interferon signaling and major histocompatibility complex (MHC) class I-mediated antigen presentation in PRC2-deficient MPNSTs (Wojcik et al., 2019). Interestingly, PRC2 regulation of genes involved in immune surveillance has previously been reported in PRC2-competent cancers. In this context, abnormally increased PRC2 activity was directly responsible for the transcriptional silencing of MHC class I-mediated antigen presentation (Burr et al., 2019). In contrast, in PRC2-deficient MPNSTs, these same MHC class I genes were not direct PRC2 targets and did not gain H3K27me3 when a functional PRC2 was restored. Instead, we find that PRC2 restoration directly downregulates hyperactive Ras signaling, which dampens STAT/IRF signaling and results in the indirect transcriptional activation of the immune-related genes. These results indicate that, while neither MEK inhibition nor immunotherapy alone would be successful, combination strategies designed to dampen hyperactivated Ras signaling while activating the immune system may be beneficial in the treatment of MPNST.

Excitingly, clinical trials designed to test these combination therapeutic strategies are in development.

Limitations of the study

We report in this study that PRC2 restoration caused indirect transcriptional activation of genes in the type I interferon signaling and antigen presentation pathways. This observation is consistent with a previous study, in which Wojcik et al. found that PRC2 loss was associated with reduction of these immune genes in patient MPNST samples (Wojcik et al., 2019). Using engineered MPNST cell lines coupled with flow cytometry, we revealed modest increases in cell-surface expression of HLA class I molecules after PRC2 restoration. This is likely due to the limitation of the *in vitro* model systems used in this study; the profound dampening of antigen presentation and interferon signaling by PRC2 inactivation in MPNST patient samples is likely further influenced by the complex tumor microenvironment, which cannot be modeled or tested in cell lines. Future studies using immune-competent animal models of SC-specific PRC2 inactivation will be useful to fully evaluate these changes. Another key limitation of our study is the inclusion of a small number of clinical samples available for transcriptomic profiling. Additional studies of larger cohorts of patients will be required to validate our observations.

STAR★METHODS

RESOURCE AVAILABILITY

Lead contact—Further information and requests for resources and reagents should be directed to and will be fulfilled by the lead contact, Jack F. Shern (john.shern@nih.gov).

Materials availability—DNA constructs and other research reagents generated by the authors wil be distributed upon request to other researchers.

Data and code availability

- All datasets used are summarized in the key resources table. Raw and processed next generation sequencing data generated for this study have been deposited in the National Center for Biotechnology Information (NCBI) gene expression omnibus (GEO) with the accession number GEO: GSE183309. This SuperSeries is composed of the following SubSeries: GSE183305, GSE183306, GSE183307, GSE183308, and GSE202671, containing related ATAC-seq, ChIP-seq, RNAseq, single-cell RNA-seq, and CUT&RUN data, respectively.

- This study did not generate any unique code.

- Any additional information required to reanalyze the data reported in this paper is available from the lead contact upon request.

EXPERIMENTAL MODEL AND SUBJECT DETAILS

Cell lines and culture conditions—MPNST cell lines, T265, S462 and sNF96.2, were kindly provided by Dr. Karlyne Reilly (Pediatric Oncology Branch, NCI) and were maintained in DMEM10 (Dulbecco's Modified Eagle Medium

supplemented with 10% fetal bovine serum and 100 U/mL penicillin and 100 μg/mL streptomycin). Cell line sNF02.2 was purchased from ATCC (Manassas, VA) and maintained in DMEM10. Sporadic MPNST cell line STS-26T was kindly provided by Dr. Steven Porcelli (Albert Einstein College of Medicine) and maintained in DMEM10. Cell lines MPNST724 and ST88-14 were kindly provided by Dr. Nancy Ratner and maintained in DMEM10. NF1 patient-derived MPNST cell lines PT2002 and PT2031 were requested through The Johns Hopkins NF1 Biospecimen Repository (https://www.hopkinsmedicine.org/kimmel_cancer_center/cancers_we_treat/pediatric_oncology/research_and_clinical_trials/pratilas/nf1_biospecimen_repository.html) and kindly provided by Dr. Christine Pratilas. They were cultured in RPMI10 (RPMI 1640 medium supplemented with 10% fetal bovine serum and 100 U/mL penicillin and 100 μg/mL streptomycin). Finally, patient-derived MPNST cell line PDX was established from a primary sporadic MPNST sample in the laboratory of Dr. Rosandra Kaplan (Pediatric Oncology Branch, NCI) and kindly provided to us to be maintained in DMEM10. Lenti-X HEK293 cells were originally purchased from Takara Bio (Mountain View, CA) and maintained in DMEM10 and kindly provided by Dr. Carol Thiele's laboratory (Pediatric Oncology Branch, NCI). All cell culture was carried out in an incubator at 37°C with 5% CO_2 and routinely tested for mycoplasma contamination. Cell lines sNF02.2, sNF96.2, S462, T265 and STS-26T were characterized by the short tandem repeat (STR) analysis and their signatures matched known profiles. In addition, each cell line was subjected to exome-based sequencing and the FASTQ sequencing files were deposited and available for public use (Synapse). For the cell growth assays, the Essen IncuCyte FLR (Essen BioScience, Ann Arbor, MI) was used to monitor the cell confluency over time.

Patients—Three resected MPNST samples and one surgical biopsy from two NF1 pediatric patients (including one female and one male patient; age less than 18) were analyzed in this study. Informed consent was obtained on NCI IRB approved protocol (NCT01109394; IRB identifier 10C0086) for the tumor samples prospectively collected and included in this work.

METHOD DETAILS

Construction of the inducible expression vectors—Open reading frame (ORF) of human *SUZ12* (NM_015355, GenScript, Piscataway, NJ) was cloned into the pLVX-TetOne-Puro vector (Takara Bio) using In-Fusion HD (Takara Bio), following the manufacturer's manual. MPNST cell lines were infected with lentiviral particles generated using either pLVX-TetOne-Puro-SUZ12 or empty vector (pLVX-TetOne-Puro-EV), followed by puromycin selection (STS-26T: 5 μg/mL, T265: 1 μg/mL, ST88-14: 5 μg/mL, and PT2002: 1 μg/mL). Various doses of doxycycline (Dox) were used in these cells to induce various levels of SUZ12 expression. To profile the epigenetic alterations caused by PRC2 restoration in these cells, Dox concentration of 0.5 μg/mL was chosen for the reason that it can induce SUZ12 re-expression to its level shown in a PRC2-WT cell line, STS-26T (Figure S1B). For the Dox dose-dependent growth assay, low and high doses used are listed here: T265 (0.1 μg/mL and 0.5 μg/mL, respectively), ST88-14 (0.05 μg/mL and 0.1 μg/mL, respectively) and PT2002 (0.02 μg/mL and 0.05 μg/mL, respectively). Without further specification, all experiments with a functional PRC2 restored used 0.5 μg/mL Dox for 5 day. Media with Dox was replenished every two days.

Protein isolation, histone extraction and western blotting analysis—To assess protein levels, samples were harvested from cultured cell lines for immunoblotting analysis. Whole cell protein lysate was collected from lysed cells resuspended in 1x Cell Lysis Buffer (Cell Signaling Technology, Danvers, MA) supplemented with 1x protease inhibitor cocktail (Thermo Fisher, Waltham, MA). Protein concentration was assessed using Bradford assay dye (Bio-Rad, Hercules, CA) and read in the SpectraMax M3 microplate reader (Molecular Devices, San Jose, CA). Protein samples were then denatured in 1x SDS Sample Loading Buffer (Invitrogen) at 95°C for 5 min and 1.5–7.5 μg of total protein was separated using an SDS-PAGE system by size via gel electrophoresis. Protein was transferred to a nitrocellulose membrane using the Trans-Blot Turbo Transfer system (Bio-Rad). The membrane was subsequently blocked with 5% non-fat milk dissolved in 0.1% TBS-tween for 1 h at room temperature followed by incubation with primary antibody overnight at 4°C. The membrane was then washed with 0.1% TBS-tween 4 times for 10 min each time followed by one-hour room temperature secondary antibody incubation. The membrane was developed using SuperSignal West Pico chemiluminescent substrate (Thermo Fisher), SuperSignal West Femto chemiluminescent substrate (Thermo Fisher), or Clarity Max Western ECL Substrate (Bio-Rad) to be visualized by chemiluminescence imaging system (ChemiDoc, Bio-Rad). To detect histone proteins, harvested cell pellets were used to isolate total histones using Total Histone Extraction Kit (Epigentek, Farmingdale, NY) according to the manufacturer's instruction. Concentration of histone extract was assessed using Bradford assay, and histone protein was denatured in 1x SDS Sample Loading Buffer before being separated by gel electrophoresis. Detection of histone protein was achieved in a similar process as total protein described above. Protein band intensity was assessed and quantified using the Quantity One software (Bio-Rad).

Co-immunoprecipitation—Primary antibodies against FOXC1, EZH2, SUZ12 and IgG isotype control were incubated overnight with Dynabeads M-280 Sheep anti-Rabbit IgG magnetic beads (Invitrogen) followed with washing using Washing Buffer (50 mM Tris-HCl pH 7.5, 137 mM NaCl, 0.005 Triton X-100, 1 mM EDTA, de-ionized H_2O). Whole cell lysates from cultured cells were incubated with the primary antibody-bound magnetic beads under continuous rotation at 4°C for 4 h. Excessive unbound protein was cleared from the beads by washing. After 5 rounds of washing with Washing Buffer, the co-IP products were eluted from the beads by boiling in 1x SDS Loading Buffer at 99°C for 5 min with shaking at 1000 rpm. Three percent of the whole cell lysate input was loaded alongside co-IP products for gel electrophoresis. Nitrocellulose membrane bound with protein was incubated with the corresponding primary antibodies followed by incubation with the sheep-against rabbit light-chain specific secondary antibody. Developed membrane was imaged using ChemiDoc (Bio-Rad) as described above.

RNAseq—Total RNA was isolated and subjected to transcriptomic profiling from MPNST cells that were constructed with the inducible expression vector after they were treated with or without 0.5 μg/mL of Dox for 5 consecutive days. Total RNA extraction was carried out using the RNeasy Mini Kit (Qiagen, Hilden, Germany), per manufacturer's direction. Quality and quantity of RNA samples were assessed using the Agilent 2100 Bioanalyzer at the Genomics Core of the Center for Cancer Research (CCR) in NIH. Samples with an RNA

integrity number that was larger than 9.0 were further processed for library construction and sequencing at the sequencing facility at Frederick National Laboratory for Cancer Research (CCRSF). Strand-specific transcriptomic sequencing library was constructed by using the TruSeq Stranded Library Preparation Kit (Illumina, San Diego, CA) following the manufacturer's instruction. Samples were pooled and sequenced on a HiSeq4000 sequencer for paired-end sequencing with a read length of 150 base pair (bp).

Quantitative real-time PCR (qRT-PCR)—Total RNA was converted to cDNA using the High-Capacity RNA-to-cDNA kit (Thermo Fisher). To measure the relative mRNA levels of *FOXC1*, *SMAD3*, *TGFBI*, and *RUNX2*, quantitative PCR was performed in a 384-well plate using the CFX real-time PCR system (Bio-Rad) as previously described (Zhang et al., 2017). The mRNA level of housekeeping gene *HPRT1* was used as the internal control for normalization.

ChIP-seq—ChIP was performed using the ChIP-IT High Sensitivity kit (Active Motif, Carlsbad, CA), following the manufacturer's manual. Briefly, formaldehyde-(1%, room temperature, 15 min) fixed chromatin was sheared to fragments of 200–1000 bp with the EpiShear Probe Sonicator (Active Motif). T265 cells were sonicated at 30% amplitude, pulse for 20 s on and 40 s off for a total sonication "on" time of 15 min; ST88-14 and PT2002 cells were sonicated at 30% amplitude, pulse for 20 s on and 40 s off for a total sonication "on" time of 16 min. Sheared chromatin was immunoprecipitated with antibodies against H3K27me3, H3K27ac, H3K4me3 or FOXC1 overnight at 4°C, followed by agarose protein A/G beads enrichment and DNA purification. To date, genome wide FOXC1 binding has not been profiled. A commercially available FOXC1 antibodies was used as it was tested suitable for ChIP-seq assays by ChIP-western blotting and peak calling. Drosophila chromatin (Active Motif) was added to the ChIP reaction and an antibody against Drosophila-specific histone variant H2Av (Active Motif) was included in the pull down. ChIP DNA library was prepared at the CCRSF using TruSeq ChIP Library Prep Kit (Illumina, cat. IP-202-1012) and sequenced on a NextSeq platform for single-end sequencing with a read length of 76 bp. About 25-30 million base-pairs uniquely mapped reads were generated from each sample.

CUT&RUN and sequencing—Cleavage Under Targets and Release Using Nuclease (CUT&RUN) was performed using the CUT&RUN assay kit (Cell Signaling Technology), following the manufacturer's protocol. Briefly, 100,000 cells were fixed with formaldehyde (0.1%, room temperature, 2 min, with rotation) before binding with the activated Concanavalin A Beads. Antibody against H3K27ac (Active Motif) was added to the cell:bead suspension, followed by the addition of pAG-MNase enzyme, which was subsequently activated by calcium to digest the DNA. The reaction was sequestered using the Stop Buffer that was supplemented with 5 pg of S. cerevisiae yeast spike-in DNA and the DNA was extracted and purified. The input DNA was sheared to 100-600 bp fragments using a sonicator (Covaris, Woburn, Massachusetts) before purification. CUT&RUN library was prepared using the SimpleChIP ChIP-seq DNA library Prep Kit for Illumina (Cell Signaling Technology) with Simple ChIP ChIP-seq Multiplex Oligos (Cell Signaling

Technology) and sequences on a NextSeq platform for paired-end sequencing with a read length of 75 bp.

ATAC-seq—ATAC-seq was performed as previously described (Corces et al., 2017; Liu et al., 2020). In brief, 50000 cells were seeded in DMEM10 with or without Dox for 5 days, and 50000 cells were pelleted in cold PBS. The cells were lysed by resuspending in 100 μL cold ATAC-resuspension buffer (RSB, 0.1% NP40, 0.1% Tween 20, and 0.01% Digitonin) and incubated on ice for 3 min. The lysis was washed in 1.4 mL of cold ATAC-wash buffer (0.1% Tween 20) and the pelleted nuclei was resuspended in 100 μL of transposition mixture (50 μL 2x TD buffer, 5 μL transposase (100nM final), 33 μL PBS, 1 μL 1% digitonin, 1 μL 10% Tween 20, 5 μL H_2O. After incubation at 37°C for 30 min in a thermomixer (Eppendorf, Enfield, CT) at 1000 rpm, the reaction was cleaned up with a Zymo DNA Clean and Concentrator-5 Kit (Zymo Research, Irvine, CA) and the DNA was eluted in 21 μL elution buffer. Nextera DNA Library Prep kit (Illumina) was used for ATAT sequencing library preparation, according to the manufacturer's protocol. The amplified library was right size selected using SPRIselect reagent (Beckman, Brea, CA) following the instruction. ATAC libraries were sequenced on an Illumina NextSeq machine (paired-end 75-bp reads). The Fastq files were processed using Encode ATAC_DNase_pipelines (https://github.com/kundajelab/atac_dnase_pipelines) installed on the NIH biowulf cluster (https://hpc.nih.gov/apps/atac_dnase_pipelines.html).

Antibodies—Antibodies used for western blotting (WB), co-immunoprecipitation (co-IP), chromatin-immunoprecipitation (ChIP) and flow cytometry assays were obtained from different companies with different dilutions used for different assays. Their source and specific dilutions are listed in Table S7.

Transient transfection—Transient transfection was performed using Lipofectamine RNAiMAX (Invitrogen, Carlsbad, CA) following a reverse transfection protocol. Briefly, lipofectamine and RNAi duplex were separately diluted in Opti-MEM and then mixed together and incubated at room temperature for 20 min. The mixture was added to the cell culture plate followed by the addition of counted cells. The following small interfering RNAs (siRNA) were purchased from Qiagen (Germantown, MD): AllStars Negative control siRNA (cat. 1027281), siFOXC1-1 (cat. SI00026138), siFOXC1-5 (cat. SI03037713), siHOXB8-4 (cat. SI00440685), siHOXB8-6 (cat. SI04311916).

Customized siRNA library screening—A customized siRNA library was assembled by picking 3 individual siRNA that target different regions of the candidate CRC transcription factor. This was done through the GeneGlobe gene-specific product lookup tool on the Qiagen website (https://geneglobe.qiagen.com/product-groups/flexiplate-sirna), and all siRNA products were purchased from Qiagen on a 384-well plate in 0.1 nmol quantities. The stock siRNA (10 μM) was created by adding 10 μL of RNase-free H_2O directly into the product and a working solution of 1 μM was created with further dilution. The siRNA used for the screen was diluted in Opti-MEM to 133.3 nM and 10 μL of this siRNA dilution was mixed with 10 μL of lipofectamine RNAiMAX diluted in Opti-MEM directly in a 384-well cell culture plate. A reverse transfection protocol was followed. Cell confluency

and morphology were assessed in real time using the Incucyte S3 live cell analysis system (Essen BioScience) for 96 h. Four days after the transfection, cell viability was assessed by using MTS assay with CellTiter 96 AQueous One Solution (Promega, Madison, WI), following the manufacturer's instructions. The median percentage reduction in signal from control siRNA was calculated and visualized in R.

CRISPR-Cas9 mediated gene knockout—To generate MPNST cells that expressed an inducible Cas9 protein, they were transduced with the lentivirus of Edit-R Inducible Lentiviral Cas9 (Dharmacon, Waltham, MA) followed with antibiotic selection by blasticidin (Invitrogen). These cells expressed Cas9 when induced with Dox (0.5 μg/mL). Two guide RNAs (gRNAs) that target the exon of human *FOXC1* gene or the first exon of human *HOXB8* gene were designed using the online tool offered by Dharmacon. They were synthesized and cloned onto the pLentiGuide-Puro vector (GenScript, Piscataway NJ) to be packaged into lentivirus using the Lenti-X HEK293 cells. The above mentioned Dox-inducible Cas9-expressing MPNST cells were transduced with the lentivirus of these gRNAs and selected with puromycin (Invitrogen). Gene-editing was enabled by Dox treatment and the elimination of target protein was confirmed by western blotting after 5-7 days post treatment.

Soft agar clonogenic assay—To assess effects of *SUZ12 restoration, FOXC1* knockout and *HOXB8* knockout on anchorage independent cell growth, 1.5×10^5 cells stably transfected with Dox-inducible *SUZ12* expression constructs, Dox-inducible Cas9 and two gRNAs targeting *FOXC1* and *HOXB8* were cultured in 0.7% top agarose in DMEM10 on a layer of 1.4% bottom agarose in DMEM10 to prevent the adhesion of cells to the culture plates. Medium was changed twice a week with or without 0.5 μg/mL Dox. Colonies with a diameter approximately 200 μM were counted under a microscope after 4 weeks. Representative colonies were imaged using a Nikon Eclipse TE300 microscope (Nikon, Melville, NY).

Flow cytometry—Dox-inducible *SUZ12*-expressing cell, T265, were seeded then treated with Dox (0.5 μg/mL) the following day. Two million cells treated with or without Dox were harvested and washed once with flow staining buffer (FSB, PBS supplemented with 2% FBS and 1 mM EDTA) and blocked with anti-Fc receptor (Biolegend) at room temperature for 5 min. One million cells from each condition were stained with PE anti-human HLA-A,B,C or IgG isotype and the fixable viability dye eFluor 506, which were diluted with FSB at room temperature for 12 min. A separate half million cells were incubated on a heat block at 65°C for 1 min to kill the cells, then mixed with the remaining half million cells and stained with the fixable viability dye eFluor 506 alone for compensation. A separate million cells were stained with PE anti-human HLA-A,B,C alone for compensation. Post staining, cells were washed twice with FSB followed by resuspension in 300 μL of FSB and ready for flow cytometry. The LSRFortessa (BD, Franklin Lakes, NJ) flow cytometer was used to assess the fluorescent intensity of MPNST cells stained for human MHC I molecules. Cells were gated to retain live, single cells for downstream analysis of the protein of interest in FlowJo software (BD). The stacked intensity of HLA-A,B,C was visualized in FlowJo.

Single-cell RNAseq—Patient MPNST samples were directly collected from the operating room in the Center for Clinical Research of the National Institutes of Health and immediately processed in a laminar flow hood. The tumor was minced into 1 mm^3 cubes in tumor dissociation media {DMEM10, collagenase I (STEMCELL Technologies, Vancouver, Canada), dispase II (MilliporeSigma, St. Louis, MO), and DNase I (Invitrogen)}, and transferred to a gentleMACS C Tube (Miltenyl Biotec, Bergisch Gladbach, Germany) and dissociated on a gentle-MACS dissociator (Miltenyl Biotec) followed by shaking at 200 rpm at 37°C for 40 min. The dissociated tumor cells were pushed through a 40 mm cell strainer with a syringe plunge, and the cell strainer was rinsed twice with DMEM10. The cells were washed with PBS and counted using the AO/PI viability dye (Nexcelom, Lawrence, MA) in an automated cell counter, Cellometer Auto 2000 (Nexcelom) or LunaFL (Logos Biosystems, Annandale, VA). Ten thousand live cells per capture lane were subsequently captured by the Chromium Controller (10x Genomics, Pleasanton, CA), aiming to capture 6000 live cells per lane, using the v3 reagent for library preparation, following the manufacturer's instructions. Sequencing was done on the Illumina sequencer NextSeq550, aiming for >50000 reads per cell.

QUANTIFICATION AND STATISTICAL ANALYSIS

RNAseq data analysis—Reads of the samples were trimmed for adapters and low-quality bases using Trimmomatic (Bolger et al., 2014) before alignment with the reference genome (Human – hg19) and the annotated transcripts using STAR (Dobin et al., 2013). The average mapping rate of all samples was 97%. Unique alignment was above 86%. There were 1.94–4.20% unmapped reads. The mapping statistics were calculated using Picard software. The samples had 0.83% ribosomal bases. Percent coding bases were between 56 and 61%. Percent UTR bases were 28–34%, and mRNA bases were between 87 and 94% for all the samples. Library complexity was measured in terms of unique fragments in the mapped reads using Picard's MarkDuplicate utility. The samples had 68-78% non-duplicate reads. In addition, the gene expression quantification analysis was performed for all samples using STAR/RSEM (Li and Dewey, 2011) tools. The raw count was used in DESeq2 (Love et al., 2014) for differentially expressed gene analysis. Statistical results of gene expression from DESeq2 were used in gene set enrichment analysis (GSEA) and a false-discovery rate of less than 0.25 was considered a significant enrichment. Gene Ontology (GO) Enrichment analysis was performed using the list of differentially expressed genes against all GO terms. The normalized count, specifically fragments per kilobase of transcript per million mapped reads (FPKM), was used for data visualization in heatmaps. R package ComplexHeatmap (Gu et al., 2016) was used to generate heatmaps in R (version 3.6.1). Raw RNAseq results were aligned to human genome hg19 and converted to bigwig files using deeptools (Ramírez et al., 2016) for visualization in the IGV genome browser (Robinson et al., 2011) together with ChIP-seq data.

ChIP-seq and CUT&RUN data analysis—ChIP and CUT&RUN enriched DNA reads were trimmed for adapters using Trimmomatic software before the alignment. The trimmed reads were aligned to the reference human genome (version hg19) using BWA (Li and Durbin, 2009). Duplicated reads were discarded. Reads aligned to regions of the hg19 genome known to be prone to artifactual increased alignments were removed. For sample

visualization in IGV, bam files that contained the alignment reads were carried into deepTools for the generation of coverage track (bigwig files) using the bamCoverage function (Ramírez et al., 2016). Read counts aligned to human (hg19) and Drosophila (dm3) genomes were calculated for the normalization of ChIP-seq spike in. Read counts aligned to human (hg19) and S. cerevisiae yeast genomes were calculated for the normalization of CUT&RUN spike in. The coverage was calculated by extending the reads to the average size, which was measured by Agilent Bioanalyzer (Agilent, Santa Clara, CA), and counting the number of reads per bin, where bins were short consecutive counting windows of 25 bp. These bigwig files were also used to plot heatmaps using deepTools and the metagene plot using NGSplot (Shen et al., 2014).

ChIP-seq read density values were normalized per million mapped reads. High-confidence peaks were identified by MACS (Zhang et al., 2008) (version 2.2.6) with the narrow algorithm for FOXC1 and H3K4me3 and broad algorithm for H3K27me3 and H3K27ac. Overlapped H3K27me3 peaks were identified using the H3K27me3 peak files of all three inducible cell lines in the +Dox condition in BEDTools (https://bedtools.readthedocs.io/en/latest/index.html) and BEDOPS (Neph et al., 2012). Bivalent domains marked by both H3K27me3 and H3K4me3 are poised for rapid transcriptional control during development (Bernstein et al., 2006). H3K27me3 and H3K4me3 peaks were overlapped at these bivalent sites in the each of the three Dox-induced cell lines. Cell specific bivalent domains were defined if a restored H3K27me3 peak overlapped with H3K4me3 peak within a given MPNST cell line. Intersection of the peaks from the three lines demonstrated 850 common bivalent genomic sites observed in the three cell lines. FOXC1 peaks were segmented into three categories: promoters (within +/− 1000 bp from the transcription starting site), enhancer-bound (overlapped with enhancer bed file in BEDOPS) and others. Peaks were annotated in HOMER (Heinz et al., 2010) with the promoter defined as transcription starting site +/− 1000 bp. Peak-associated genes were used for GO analysis and visualization in R package ReactomePA (Yu and He, 2016). Enrichment of known and *de novo* motifs were first identified using HOMER (Heinz et al., 2010) and confirmed with in-house algorithm.

Enhancers were identified using the Rank Ordering of Super-Enhancer (ROSE) software (Lovén et al., 2013; Whyte et al., 2013) and distal (>2500 bp from transcription starting site) H3K27ac peaks. Enhancer constituents were stitched together if clustered within a distance of 12.5 kb. The enhancers were classified into typical and super enhancers based on a cutoff at the inflection point (where tangent slope = 1) in the rank-ordered H3K27ac ChIP-seq signal, which was normalized to input signal. To identify candidate core transcription factors, CRCmapper was adopted to find autoregulated super enhancer-driven expressed transcription factors (Saint-André et al., 2016). MPNST-specific core transcription factors were defined by comparing published MPNST tissue RNAseq (Lee et al., 2014) and in-house generated MPNST cell line RNAseq data with a panel of normal tissue controls(Chang et al., 2016) to find those significantly highly expressed in MPNSTs (p < 0.05 by Student's t-test). The predicted inter-connected transcriptional regulations through MPNST-specific autoregulated super enhancer-driven transcription factors were visualized using the R package circlize (Gu et al., 2014).

Single-cell RNAseq data analysis—The single-cell RNA sequencing results were analyzed preliminarily with the Cell Ranger pipeline offered by the 10X Genomics. The generated count matrix was used in downstream analysis in Seurat 4.0. Briefly, gene counts were normalized and scaled before dimensional reduction for the clustering analysis. Cluster biomarkers were identified by finding the differentially expressed genes in each cluster with comparison to all other clusters. For multiple sample analysis, we used the anchor-based standard integration pipeline in Seurat 4.0 (Butler et al., 2018; Stuart et al., 2019). Generally, subclones that were present in more than one sample were identified and biomarkers that were conserved in the common subclones or unique to each subclone were obtained. Cell types were manually annotated based on the expression of identified marker genes in each cluster. Using the immune cells from these MPNST single-cell datasets as a reference, we inferred copy number variation by using the R package inferCNV (inferCNV of the Trinity CTAT Project. https://github.com/broadinstitute/inferCNV).

Single-cell whole genome sequencing and data processing—To profile the genomic dynamic of tumor cells of a patient MPNST, a portion of the dissociated tumor cells from the resected primary MPNST of the first patient that were prepared for single-cell RNAseq were used for single-cell whole genome sequencing. Basically, about 600 live cells per lane were captured in the Chromium controller using the Chromium Chip single-cell CNV chemistry for library preparation (10x Genomics). The library was sequenced on an Illumina NovaSeq6000 platform and a total of 1270 cells were sequenced for an average of 1.8 million reads per cell. The median estimated copy number variation resolution was 0.84 million bp. Sequencing reads were processed and analyzed using the Cell Ranger DNA analysis pipeline (10X Genomics), which included sample demultiplexing, barcode detection, read alignment, copy number estimation on single-cells and groups of cells defined by hierarchy clustering. The hierarchically clustered single-cell copy number profiling and genomic variability across the genome were visualized in Loupe scDNA Browser (10X Genomics). To definitively determine the malignant cell populations in the tumor, results from the single-cell whole genome sequencing were subsequently compared to results from the inferred copy number profiling generated from the using single-cell RNAseq results.

Construction of a normal schwann cell developmental trajectory

<u>Data download and processing:</u> Read count matrices of E9.5 neural crest cells {GSE129114 (Soldatov et al., 2019)}, E12.5/E13.5 adrenal medulla cells {GSE150150 (Furlan et al., 2017)}, and mature Schwann cells {GSE142541 (Wolbert et al., 2020)} were downloaded from the GEO database. Published cell-type annotations were used for GSE129114 (Table S9 in source publication) and GSE142451. For GSE150150, batch correction and clustering were performed using the default parameters in Seurat, and annotated cell types were identified based on marker genes employed in the source publication.

After all datasets were merged together, marker genes were derived for each cell type using the FindMarkers function in Seurat using the built-in logistic regression-based algorithm. The library size (sequencing depth in each cell), cell cycle status, and batch were used as

co-variates to estimate the p value of differential expression for each gene. Genes with an adjusted p value of less than 0.1 were retained as signature genes for each cell type, with at most 300 genes in each signature. The activity of each of the signature gene set was scored using AUCell, which is a part of the SCENIC package (Aibar et al., 2017). The AUCell activities were compared between malignant MPNST cells and normal Schwann cells from the patient MPNST single-cell dataset using two-sided Wilcoxon test.

Trajectory analysis: Since data from GSE129114 and GSE150150 represented a much greater library size than GSE142541, reads were down-sampled from both these datasets to match the library size distribution of cells in GSE142541. Monocle3 (Cao et al., 2019; Trapnell et al., 2014) was then used to construct a trajectory from the merged data, where batch correction was internally performed before pseudotime values were computed for each cell. E9.5 neural tube cells were chosen to represent the root state of the trajectory and were assigned a pseudotime value of zero.

Regulon analysis: SCENIC (Aibar et al., 2017) was used to derive regulons, i.e., a target gene set for each TF, active in each developing cell type, based on the presence of binding sites within 10 kb of the TSS of expressed genes. TFs whose mean regulon activity was at least 0.03 in at least one of the cell types were retained for further analyses.

Motif analysis in promoter and enhancers—Promoters and enhancer regions were scanned with a custom script that relied on the SPRY-SARUS motif scanner (Kulakovskiy et al., 2016). A total of 816 motifs from a merged collection of HOCOMOCO v11 and JASPAR 2020 databases were used (Fornes et al., 2020; Kulakovskiy et al., 2016). During the merging process, if the motif for the same TF was present in both collections, the HOCOMOCO motifs were retained since these are known to correlate highly with ChIP-seq peaks (Kulakovskiy et al., 2016). During the motif scan process, those TFs that had a non-zero average expression were chosen within the MPNST and Proliferating clusters.

Those genomic regions spanning 1 kb upstream and 200 bp downstream of transcription start sites were chose as promoters. The stitched H3K27ac peaks that were the output of the ROSE algorithm were used as enhancers. Motif enrichment in promoters and enhancers was separately computed but the same methodology was used for both classes of regions.

Out of the motifs in our collection, those 651 motifs whose TFs had a mean expression above zero in the MPNST and Proliferating clusters were used. For an input set of foreground genomic regions, a dinucleotide-shuffled set of background regions was generated using the Euler algorithm from TFBSTools (Tan and Lenhard, 2016). For each motif, the total number of motif matches in the foreground and background using a motif score threshold that corresponded to a p value of 10^{-4} was calculated. Then the fold-enrichment, F, for the motif was defined as the ratio between the number of binding sites in the foreground set to that of the background set. Multiple binding sites were allowed to occur in each sequence. Since the lengths of genomic regions in the foreground and background set are identically distributed, the value of F controls for the fact that super-enhancers, owing to their larger size than typical enhancers and promoters, are more likely to contain false positive binding site matches.

Statistical analysis—The statistical methods used in this study were specified in the corresponding Results and Methods sections. Statistical analysis was performed in R, Microsoft Excel, and GraphPad Prism software (GraphPad, San Diego, CA).

Supplementary Material

Refer to Web version on PubMed Central for supplementary material.

ACKNOWLEDGMENTS

REFERENCES

Aibar S, Gonzáiez-Blas CB, Moerman T, Huynh-Thu VA, Imrichova H, Hulselmans G, Rambow F, Marine JC, Geurts P, Aerts J, et al. (2017). SCENIC: single-cell regulatory network inference and clustering. Nat. Methods 14, 1083–1086. 10.1038/nmeth.4463. [PubMed: 28991892]

Ariës IM, Bodaar K, Karim SA, Chonghaile TN, Hinze L, Burns MA, Pfirrmann M, Degar J, Landrigan JT, Balbach S, et al. (2018). PRC2 loss induces chemoresistance by repressing apoptosis in T cell acute lymphoblastic leukemia. J. Exp. Med 215, 3094–3114. 10.1084/jem.20180570. [PubMed: 30404791]

Assi SA, Imperato MR, Coleman DJL, Pickin A, Potluri S, Ptasinska A, Chin PS, Blair H, Cauchy P, James SR, et al. (2019). Subtype-specific regulatory network rewiring in acute myeloid leukemia. Nat. Genet 51, 151–162. 10.1038/s41588-018-0270-1. [PubMed: 30420649]

Bernstein BE, Mikkelsen TS, Xie X, Kamal M, Huebert DJ, Cuff J, Fry B, Meissner A, Wernig M, Plath K, et al. (2006). A bivalent chromatin structure marks key developmental genes in embryonic stem cells. Cell 125, 315–326. 10.1016/j.cell.2006.02.041. [PubMed: 16630819]

Berry FB, Mirzayans F, and Walter MA (2006). Regulation of FOXC1 stability and transcriptional activity by an epidermal growth factor-activated mitogen-activated protein kinase signaling cascade. J. Biol. Chem 281, 10098–10104. 10.1074/jbc.M513629200. [PubMed: 16492674]

Bolger AM, Lohse M, and Usadel B (2014). Trimmomatic: a flexible trimmer for Illumina sequence data. Bioinformatics 30, 2114–2120. 10.1093/bioinformatics/btu170. [PubMed: 24695404]

Bracken AP, Dietrich N, Pasini D, Hansen KH, and Helin K (2006). Genome-wide mapping of Polycomb target genes unravels their roles in cell fate transitions. Genes Dev. 20, 1123–1136. 10.1101/gad.381706. [PubMed: 16618801]

Burr ML, Sparbier CE, Chan KL, Chan YC, Kersbergen A, Lam EYN, Azidis-Yates E, Vassiliadis D, Bell CC, Gilan O, et al. (2019). An evolutionarily conserved function of polycomb silences the MHC class I antigen presentation pathway and enables immune evasion in cancer. Cancer Cell 30, 385–401.e388. 10.1016/j.ccell.2019.08.008.

Bushweller JH (2019). Targeting transcription factors i— cancer - from undruggable to reality. Nat. Rev. Cancer 19, 611–624. 10.1038/s41568-019-0196-7. [PubMed: 31511663]

Butler A, Hoffman P, Smibert P, Papalexi E, and Satija R (2018). Integrating single-cell transcriptomic data across different conditions, technologies, and species. Nat. Biotechnol 36, 411–420. 10.1038/nbt.4096. [PubMed: 29608179]

Cao J, Spielmann M, Qiu X, Huang X, Ibrahim DM, Hill AJ, Zhang F, Mundlos S, Christiansen L, Steemers FJ, et al. (2019). The single-cell transcriptional landscape of mammalian organogenesis. Nature 566, 496–502. 10.1038/s41586-019-0969-x. [PubMed: 30787437]

Cauchy P, James SR, Zacarias-Cabeza J, Ptasinska A, Imperato MR, Assi SA, Piper J, Canestraro M, Hoogenkamp M, Raghavan M, et al. (2015). Chronic FLT3-ITD signaling in acute myeloid leukemia is connected to a specific chromatin signature. Cell Rep. 12, 821–836. 10.1016/j.celrep.2015.06.069. [PubMed: 26212328]

Chang W, Brohl AS, Patidar R, Sindiri S, Shern JF, Wei JS, Song YK, Yohe ME, Gryder B, Zhang S, et al. (2016). MultiDimensional ClinOmics for precision therapy of children and adolescent young adults with relapsed and refractory cancer: a report from the center for cancer research. Clin. Cancer Res 22, 3810–3820. 10.1158/1078-0432.CCR-15-2717. [PubMed: 26994145]

Chen Z, Liu C, Patel AJ, Liao CP, Wang Y, and Le LQ (2014). Cells of origin in the embryonic nerve roots for NF1-associated plexiform neurofibroma. Cancer Cell 26, 695–706. 10.1016/j.ccell.2014.09.009. [PubMed: 25446898]

Comet I, Riising EM, Leblanc B, and Helin K (2016). Maintaining cell identity: PRC2-mediated regulation of transcription and cancer. Nat. Rev. Cancer 16, 803–810. 10.1038/nrc.2016.83. [PubMed: 27658528]

Corces MR, Trevino AE, Hamilton EG, Greenside PG, Sinnott-Armstrong NA, Vesuna S, Satpathy AT, Rubin AJ, Montine KS, Wu B, et al. (2017). An improved ATAC-seq protocol reduces background and enables interrogation of frozen tissues. Nat. Methods 14, 959–962. 10.1038/nmeth.4396. [PubMed: 28846090]

De Raedt T, Beert E, Pasmant E, Luscan A, Brems H, Ortonne N, Helin K, Hornick JL, Mautner V, Kehrer-Sawatzki H, et al. (2014). PRC2 loss amplifies Ras-driven transcription and confers sensitivity to BRD4-based therapies. Nature 514, 247–251. 10.1038/nature13561. [PubMed: 25119042]

de Thé H (2018). Differentiation therapy revisited. Nat. Rev. Cancer 18, 117–127. 10.1038/nrc.2017.103. [PubMed: 29192213]

Decaesteker B, Denecker G, Van Neste C, Dolman EM, Van Loocke W, Gartlgruber M, Nunes C, De Vloed F, Depuydt P, Verboom K, et al. (2018). TBX2 is a neuroblastoma core regulatory circuitry component enhancing MYCN/FOXM1 reactivation of DREAM targets. Nat. Commun 9, 4866. 10.1038/s41467-018-06699-9. [PubMed: 30451831]

Dehner C, Moon CI, Zhang X, Zhou Z, Miller C, Xu H, Wan X, Yang K, Mashl J, Gosline SJ, et al. (2021). Chromosome 8 gain is associated with high-grade transformation in MPNST. JCI Insight 6. 10.1172/jci.insight.146351.

Dobin A, Davis CA, Schlesinger F, Drenkow J, Zaleski C, Jha S, Batut P, Chaisson M, and Gingeras TR (2013). STAR: ultrafast universal RNA-seq aligner. Bioinformatics 29, 15–21. 10.1093/bioinformatics/bts635. [PubMed: 23104886]

Dong R, Yang R, Zhan Y, Lai HD, Ye CJ, Yao XY, Luo WQ, Cheng XM, Miao JJ, Wang JF, et al. (2020). Single-cell characterization of malignant phenotypes and developmental trajectories of adrenal neuroblastoma. Cancer Cell 38, 716–733.e716. 10.1016/j.ccell.2020.08.014. [PubMed: 32946775]

Durbin AD, Zimmerman MW, Dharia NV, Abraham BJ, Iniguez AB, Weichert-Leahey N, He S, Krill-Burger JM, Root DE, Vazquez F, et al. (2018). Selective gene dependencies in MYCN-amplified neuroblastoma include the core transcriptional regulatory circuitry. Nat. Genet 50, 1240–1246. 10.1038/s41588-018-0191-z. [PubMed: 30127528]

Fornes O, Castro-Mondragon JA, Khan A, van der Lee R, Zhang X, Richmond PA, Modi BP, Correard S, Gheorghe M, Baranaši D, et al. (2020). JASPAR 2020: update of the open-access database of transcription factor binding profiles. Nucleic Acids Res. 48, D87–D92. 10.1093/nar/gkz1001. [PubMed: 31701148]

Franklin DA, James JL, Axelrod ML, and Balko JM (2020). MEK inhibition activates STAT signaling to increase breast cancer immunogenicity via MHC-I expression. Cancer Drug Resist. 3, 603–612. 10.20517/cdr.2019.109. [PubMed: 33062958]

Furlan A, Dyachuk V, Kastriti ME, Calvo-Enrique L, Abdo H, Hadjab S, Chontorotzea T, Akkuratova N, Usoskin D, Kamenev D, et al. (2017). Multipotent peripheral glial cells generate neuroendocrine cells of the adrenal medulla. Science 357. 10.1126/science.aal3753.

Ghislain J, and Charnay P (2006). Control of myelination in schwann cells: a Krox20 cis-regulatory element integrates Oct6, Brn2 and Sox10 activities. EMBO Rep. 7, 52–58. 10.1038/sj.embor.7400573. [PubMed: 16311519]

Gimple RC, and Wang X (2019). RAS: striking at the core of the oncogenic circuitry. Front. Oncol 9, 965. 10.3389/fonc.2019.00965. [PubMed: 31681559]

Gu Z, Gu L, Eils R, Schlesner M, and Brors B (2014). circlize Implements and enhances circular visualization in R. Bioinformatics 30, 2811–2812. 10.1093/bioinformatics/btu393. [PubMed: 24930139]

Gu Z, Eils R, and Schlesner M (2016). Complex heatmaps reveal patterns and correlations in multidimensional genomic data. Bioinformatics 32, 2847–2849. 10.1093/bioinformatics/btw313. [PubMed: 27207943]

Guerra SL, Maertens O, Kuzmickas R, De Raedt T, Adeyemi RO, Guild CJ, Guillemette S, Redig AJ, Chambers ES, Xu M, et al. (2020). A deregulated HOX gene Axis confers an epigenetic vulnerability in KRAS-mutant lung cancers. Cancer Cell 37, 705–719.e706. 10.1016/j.ccell.2020.03.004. [PubMed: 32243838]

Gupta RA, Shah N, Wang KC, Kim J, Horlings HM, Wong DJ, Tsai MC, Hung T, Argani P, Rinn JL, et al. (2010). Long non-coding RNA HOTAIR reprograms chromatin state to promote cancer metastasis. Nature 464, 1071–1076. 10.1038/nature08975. [PubMed: 20393566]

Hannenhalli S, and Kaestner KH (2009). The evolution of Fox genes and their role in development and disease. Nat. Rev. Genet 10, 233–240. 10.1038/nrg2523. [PubMed: 19274050]

Heinz S, Benner C, Spann N, Bertolino E, Lin YC, Laslo P, Cheng JX, Murre C, Singh H, and Glass CK (2010). Simple combinations of lineage-determining transcription factors prime cis-regulatory elements required for macrophage and B cell identities. Mol. Cell 38, 576–589. 10.1016/j.molcel.2010.05.004. [PubMed: 20513432]

Hnisz D, Abraham BJ, Lee TI, Lau A, Saint-André V, Sigova AA, Hoke HA, and Young RA (2013). Super-enhancers in the control of cell identity and disease. Cell 155, 934–947. 10.1016/j.cell.2013.09.053. [PubMed: 24119843]

Jackson BC, Carpenter C, Nebert DW, and Vasiliou V (2010). Update of human and mouse forkhead box (FOX) gene families. Hum. Genomics 4, 345–352. 10.1186/1479-7364-4-5-345. [PubMed: 20650821]

Jagalur NB, Ghazvini M, Mandemakers W, Driegen S, Maas A, Jones EA, Jaegle M, Grosveld F, Svaren J, and Meijer D (2011). Functional dissection of the Oct6 Schwann cell enhancer reveals an essential role for dimeric Sox10 binding. J. Neurosci 31, 8585–8594. 10.1523/JNEUROSCI.0659-11.2011. [PubMed: 21653862]

Jansky S, Sharma AK, Körber V, Quintero A, Toprak UH, Wecht EM, Gartlgruber M, Greco A, Chomsky E, Grünewald TGP, et al. (2021). Single-cell transcriptomic analyses provide insights into the developmental origins of neuroblastoma. Nat. Genet 53, 683–693. 10.1038/s41588-021-00806-1. [PubMed: 33767450]

Kameneva P, Artemov AV, Kastriti ME, Faure L, Olsen TK, Otte J, Erickson A, Semsch B, Andersson ER, Ratz M, et al. (2021). Single-cell transcriptomics of human embryos identifies multiple sympathoblast lineages with potential implications for neuroblastoma origin. Nat. Genet 53, 694–706. 10.1038/s41588-021-00818-x. [PubMed: 33833454]

Kim A, Stewart DR, Reilly KM, Viskochil D, Miettinen MM, and Widemann BC (2017). Malignant peripheral nerve sheath tumors state of the science: leveraging clinical and biological insights into effective therapies. Sarcoma 2017, 7429697. 10.1155/2017/7429697. [PubMed: 28592921]

Kulakovskiy IV, Vorontsov IE, Yevshin IS, Soboleva AV, Kasianov AS, Ashoor H, Ba-Alawi W, Bajic VB, Medvedeva YA, Kolpakov FA, and Makeev VJ (2016). HOCOMOCO: expansion and

enhancement of the collection of transcription factor binding sites models. Nucleic Acids Res. 44, D116–D125. 10.1093/nar/gkv1249. [PubMed: 26586801]

Laugesen A, Højfeldt JW, and Helin K (2016). Role of the polycomb repressive complex 2 (PRC2) in transcriptional regulation and cancer. Cold Spring Harb. Perspect. Med 6. 10.1101/cshperspect.a026575.

Lee W, Teckie S, Wiesner T, Ran L, Prieto Granada CN, Lin M, Zhu S, Cao Z, Liang Y, Sboner A, et al. (2014). PRC2 is recurrently inactivated through EED or SUZ12 loss in malignant peripheral nerve sheath tumors. Nat. Genet 46, 1227–1232. 10.1038/ng.3095. [PubMed: 25240281]

Li H, and Durbin R (2009). Fast and accurate short read alignment with Burrows-Wheeler transform. Bioinformatics 25, 1754–1760. 10.1093/bioinformatics/btp324. [PubMed: 19451168]

Li B, and Dewey CN (2011). RSEM: accurate transcript quantification from RNA-Seq data with or without a reference genome. BMC Bioinformatics 12, 323. 10.1186/1471-2105-12-323. [PubMed: 21816040]

Liu Z, Zhang X, Lei H, Lam N, Carter S, Yockey O, Xu M, Mendoza A, Hernandez ER, Wei JS, et al. (2020). CASZ1 induces skeletal muscle and rhabdomyosarcoma differentiation through a feed-forward loop with MYOD and MYOG. Nat. Commun 11, 911. 10.1038/s41467-020-14684-4. [PubMed: 32060262]

Love MI, Huber W, and Anders S (2014). Moderated estimation of fold change and dispersion for RNA-seq data with DESeq2. Genome Biol. 15, 550. 10.1186/s13059-014-0550-8. [PubMed: 25516281]

Lovén J, Hoke HA, Lin CY, Lau A, Orlando DA, Vakoc CR, Bradner JE, Lee TI, and Young RA (2013). Selective inhibition of tumor oncogenes by disruption of super-enhancers. Cell 153, 320–334. 10.1016/j.cell.2013.03.036. [PubMed: 23582323]

Ma KH, Hung HA, Srinivasan R, Xie H, Orkin SH, and Svaren J (2015). Regulation of peripheral nerve myelin maintenance by gene repression through polycomb repressive complex 2. J. Neurosci 35, 8640–8652. 10.1523/JNEUROSCI.2257-14.2015. [PubMed: 26041929]

Ma KH, Hung HA, and Svaren J (2016). Epigenomic regulation of schwann cell reprogramming in peripheral nerve injury. J. Neurosci 36, 9135–9147. 10.1523/JNEUROSCI.1370-16.2016. [PubMed: 27581455]

Ma KH, Duong P, Moran JJ, Junaidi N, and Svaren J (2018). Polycomb repression regulates Schwann cell proliferation and axon regeneration after nerve injury. Glia 66, 2487–2502. 10.1002/glia.23500. [PubMed: 30306639]

Mirsky R, and Jessen KR (1996). Schwann cell development, differentiation and myelination. Curr. Opin. Neurobiol 6, 89–96. 10.1016/s0959-4388(96)80013-4. [PubMed: 8794046]

Mirsky R, Stewart HJ, Tabernero A, Bradke F, Brennan A, Dong Z, and Jessen KR (1996). Development and differentiation of Schwann cells. Rev. Neurol. (Paris) 152, 308–313. [PubMed: 8881421]

Neph S, Kuehn MS, Reynolds AP, Haugen E, Thurman RE, Johnson AK, Rynes E, Maurano MT, Vierstra J, Thomas S, et al. (2012). BEDOPS: high-performance genomic feature operations. Bioinformatics 28,1919–1920. 10.1093/bioinformatics/bts277. [PubMed: 22576172]

Pasini D, Bracken AP, Jensen MR, Lazzerini Denchi E, and Helin K (2004). Suz12 is essential for mouse development and for EZH2 histone methyltransferase activity. EMBO J. 23, 4061–4071. 10.1038/sj.emboj.7600402. [PubMed: 15385962]

Pierrou S, Hellqvist M, Samuelsson L, Enerbäck S, and Carlsson P (1994). Cloning and characterization of seven human forkhead proteins: binding site specificity and DNA bending. EMBO J. 13, 5002–5012. [PubMed: 7957066]

Piunti A, Rossi A, Cerutti A, Albert M, Jammula S, Scelfo A, Cedrone L, Fragola G, Olsson L, Koseki H, et al. (2014). Polycomb proteins control proliferation and transformation independently of cell cycle checkpoints by regulating DNA replication. Nat. Commun 5, 3649. 10.1038/ncomms4649. [PubMed: 24728135]

Ramírez F, Ryan DP, Grüning B, Bhardwaj V, Kilpert F, Richter AS, Heyne S, Dündar F, and Manke T (2016). deepTools2: a next generation web server for deep-sequencing data analysis. Nucleic Acids Res. 44, W160–W165. 10.1093/nar/gkw257. [PubMed: 27079975]

Ran L, Chen Y, Sher J, Wong EWP, Murphy D, Zhang JQ, Li D, Deniz K, Sirota I, Cao Z, et al. (2018). FOXF1 defines the core-regulatory circuitry in gastrointestinal stromal tumor. Cancer Discov. 8, 234–251. 10.1158/2159-8290.CD-17-0468. [PubMed: 29162563]

Ray PS, Wang J, Qu Y, Sim MS, Shamonki J, Bagaria SP, Ye X, Liu B, Elashoff D, Hoon DS, et al. (2010). FOXC1 is a potential prognostic biomarker with functional significance in basal-like breast cancer. Cancer Res. 70, 3870–3876. 10.1158/0008-5472.CAN-09-4120. [PubMed: 20406990]

Reiprich S, Kriesch J, Schreiner S, and Wegner M (2010). Activation of Krox20 gene expression by Sox10 in myelinating Schwann cells. J. Neurochem 112, 744–754. 10.1111/j.1471-4159.2009.06498.x. [PubMed: 19922439]

Ren G, Baritaki S, Marathe H, Feng J, Park S, Beach S, Bazeley PS, Beshir AB, Fenteany G, Mehra R, et al. (2012). Polycomb protein EZH2 regulates tumor invasion via the transcriptional repression of the metastasis suppressor RKIP in breast and prostate cancer. Cancer Res. 72, 3091–3104. 10.1158/0008-5472.CAN-11-3546. [PubMed: 22505648]

Rice R, Rice DP, Olsen BR, and Thesleff I (2003). Progression of calvarial bone development requires Foxc1 regulation of Msx2 and Alx4. Dev. Biol 262, 75–87. 10.1016/s0012-1606(03)00355-5. [PubMed: 14512019]

Robinson JT, Thorvaldsdóttir H, Winckler W, Guttman M, Lander ES, Getz G, and Mesirov JP (2011). Integrative genomics viewer. Nat. Biotechnol 29, 24–26. 10.1038/nbt.1754. [PubMed: 21221095]

Saint-André V, Federation AJ, Lin CY, Abraham BJ, Reddy J, Lee TI, Bradner JE, and Young RA (2016). Models of human core transcriptional regulatory circuitries. Genome Res. 26, 385–396. 10.1101/gr.197590.115. [PubMed: 26843070]

Serresi M, Gargiulo G, Proost N, Siteur B, Cesaroni M, Koppens M, Xie H, Sutherland KD, Hulsman D, Citterio E, et al. (2016). Polycomb repressive complex 2 is a barrier to KRAS-driven inflammation and epithelial-mesenchymal transition in non-small-cell lung cancer. Cancer Cell 29,17–31. 10.1016/j.ccell.2015.12.006. [PubMed: 26766588]

Shang YK, Li C, Liu ZK, Kong LM, Wei D, Xu J, Wang ZL, Bian H, and Chen ZN (2018). System analysis of the regulation of the immune response by CD147 and FOXC1 in cancer cell lines. Oncotarget 9, 12918–12931. 10.18632/oncotarget.24161. [PubMed: 29560120]

Shen L, Shao N, Liu X, and Nestler E (2014). ngs.plot: quick mining and visualization of next-generation sequencing data by integrating genomic databases. BMC Genomics 15, 284. 10.1186/1471-2164-15-284. [PubMed: 24735413]

Soldatov R, Kaucka M, Kastriti ME, Petersen J, Chontorotzea T, Englmaier L, Akkuratova N, Yang Y, Haring M, Dyachuk V, et al. (2019). Spatiotemporal structure of cell fate decisions in murine neural crest. Science 364. 10.1126/science.aas9536.

Somerville TD, Wiseman DH, Spencer GJ, Huang X, Lynch JT, Leong HS, Williams EL, Cheesman E, and Somervaille TC (2015). Frequent derepression of the mesenchymal transcription factor gene FOXC1 in acute myeloid leukemia. Cancer Cell 28, 329–342. 10.1016/j.ccell.2015.07.017. [PubMed: 26373280]

Spyra M, Kluwe L, Hagel C, Nguyen R, Panse J, Kurtz A, Mautner VF, Rabkin SD, and Demestre M (2011). Cancer stem cell-like cells derived from malignant peripheral nerve sheath tumors. PLoS One 6, e21099. 10.1371/journal.pone.0021099. [PubMed: 21695156]

Stolt CC, and Wegner M (2016). Schwann cells and their transcriptional network: evolution of key regulators of peripheral myelination. Brain Res. 1641, 101–110. 10.1016/j.brainres.2015.09.025. [PubMed: 26423937]

Struntz NB, Chen A, Deutzmann A, Wilson RM, Stefan E, Evans HL, Ramirez MA, Liang T, Caballero F, Wildschut MHE, et al. (2019). Stabilization of the Max homodimer with a small molecule attenuates Myc-driven transcription. Cell Chem. Biol 26, 711–723.e714. 10.1016/j.chembiol.2019.02.009. [PubMed: 30880155]

Stuart T, Butler A, Hoffman P, Hafemeister C, Papalexi E, Mauck WM, Hao Y, Stoeckius M, Smibert P, and Satija R (2019). Comprehensive integration of single-cell data. Cell 177, 1888–1902.e1821. 10.1016/j.cell.2019.05.031. [PubMed: 31178118]

Sun J, Ishii M, Ting MC, and Maxson R (2013). Foxc1 controls the growth of the murine frontal bone rudiment by direct regulation of a Bmp response threshold of Msx2. Development 140, 1034–1044. 10.1242/dev.085225. [PubMed: 23344708]

Sun D, Xie XP, Zhang X, Wang Z, Sait SF, Iyer SV, Chen YJ, Brown R, Laks DR, Chipman ME, et al. (2021). Stem-like cells drive NF1-associated MPNST functional heterogeneity and tumor progression. Cell Stem Cell. 10.1016/j.stem.2021.04.029.

Tan G, and Lenhard B (2016). TFBSTooioconductorconductor package for transcription factor binding site analysis. Bioinformatics 32, 1555–1556. 10.1093/bioinformatics/btw024. [PubMed: 26794315]

Taube JH, Herschkowitz JI, Komurov K, Zhou AY, Gupta S, Yang J, Hartwell K, Onder TT, Gupta PB, Evans KW, et al. (2010). Core epithelial-to-mesenchymal transition interactome gene-expression signature is associated with claudin-low and metaplastic breast cancer subtypes. Proc. Natl. Acad. Sci. USA 107, 15449–15454. 10.1073/pnas.1004900107. [PubMed: 20713713]

Tee WW, Shen SS, Oksuz O, Narendra V, and Reinberg D (2014). Erk1/2 activity promotes chromatin features and RNAPII phosphorylation at developmental promoters in mouse ESCs. Cell 156, 678–690. 10.1016/j.cell.2014.01.009. [PubMed: 24529373]

Trapnell C, Cacchiarelli D, Grimsby J, Pokharel P, Li S, Morse M, Lennon NJ, Livak KJ, Mikkelsen TS, and Rinn JL (2014). The dynamics and regulators of cell fate decisions are revealed by pseudotemporal ordering of single cells. Nat. Biotechnol 32, 381–386. 10.1038/nbt.2859. [PubMed: 24658644]

Tribulo C, Aybar MJ, Nguyen VH, Mullins MC, and Mayor R (2003). Regulation of Msx genes by a Bmp gradient is essential for neural crest specification. Development 130, 6441–6452. 10.1242/dev.00878. [PubMed: 14627721]

Whyte WA, Orlando DA, Hnisz D, Abraham BJ, Lin CY, Kagey MH, Rahl PB, Lee TI, and Young RA (2013). Master transcription factors and mediator establish super-enhancers at key cell identity genes. Cell 153, 307–319. 10.1016/j.cell.2013.03.035. [PubMed: 23582322]

Wojcik JB, Marchione DM, Sidoli S, Djedid A, Lisby A, Majewski J, and Garcia BA (2019). Epigenomic reordering induced by polycomb loss drives oncogenesis but leads to therapeutic vulnerabilities in malignant peripheral nerve sheath tumors. Cancer Res. 79, 3205–3219. 10.1158/0008-5472.CAN-18-3704. [PubMed: 30898839]

Wolbert J, Li X, Heming M, Mausberg AK, Akkermann D, Frydrychowicz C, Fledrich R, Groeneweg L, Schulz C, Stettner M, et al. (2020). Redefining the heterogeneity of peripheral nerve cells in health and autoimmunity. Proc. Natl. Acad. Sci. USA 117, 9466–9476. 10.1073/pnas.1912139117. [PubMed: 32295886]

Xie H, Xu J, Hsu JH, Nguyen M, Fujiwara Y, Peng C, and Orkin SH (2014). Polycomb repressive complex 2 regulates normal hematopoietic stem cell function in a developmental-stage-specific manner. Cell Stem Cell 14, 68–80. 10.1016/j.stem.2013.10.001. [PubMed: 24239285]

Yohe ME, Gryder BE, Shern JF, Song YK, Chou HC, Sindiri S, Mendoza A, Patidar R, Zhang X, Guha R, et al. (2018). MEK inhibition induces MYOG and remodels super-enhancers in RAS-driven rhabdomyosarcoma. Sci. Transl. Med 10. 10.1126/scitranslmed.aan4470.

Yu G, and He QY (2016). ReactomePA: an R/Bioconductor package for reactome pathway analysis and visualization. Mol. Biosyst 12,477–479. 10.1039/c5mb00663e. [PubMed: 26661513]

Zhang Y, Liu T, Meyer CA, Eeckhoute J, Johnson DS, Bernstein BE, Nusbaum C, Myers RM, Brown M, Li W, and Liu XS (2008). Model-based analysis of ChIP-seq (MACS). Genome Biol. 9, R137. 10.1186/gb-2008-9-9-r137. [PubMed: 18798982]

Zhang M, Wang Y, Jones S, Sausen M, McMahon K, Sharma R, Wang Q, Belzberg AJ, Chaichana K, Gallia GL, et al. (2014). Somatic mutations of SUZ12 in malignant peripheral nerve sheath tumors. Nat. Genet 46, 1170–1172. 10.1038/ng.3116. [PubMed: 25305755]

Zhang X, Cook KL, Warri A, Cruz IM, Rosim M, Riskin J, Helferich W, Doerge D, Clarke R, and Hilakivi-Clarke L (2017). Lifetime genistein intake increases the response of mammary tumors to tamoxifen in rats. Clin. Cancer Res 23, 814–824. 10.1158/1078-0432.CCR-16-1735. [PubMed: 28148690]

Zhang X, Murray B, Mo G, and Shern JF (2020). The role of polycomb repressive complex in malignant peripheral nerve sheath tumor. Genes 11. 10.3390/genes11030287.

Zhu X, Wei L, Bai Y, Wu S, and Han S (2017). FoxC1 promotes epithelial-mesenchymal transition through PBX1 dependent transactivation of ZEB2 in esophageal cancer. Am. J. Cancer Res 7, 1642–1653. [PubMed: 28861321]

Highlights

- PRC2 loss activates bivalent genes via transcriptional recruitment of active enhancers

- PRC2 loss activates core TFs required to sustain the MPNST oncogenic program

- PRC2-null MPNSTs mimic Schwann cell progenitors and reduce antigen presentation

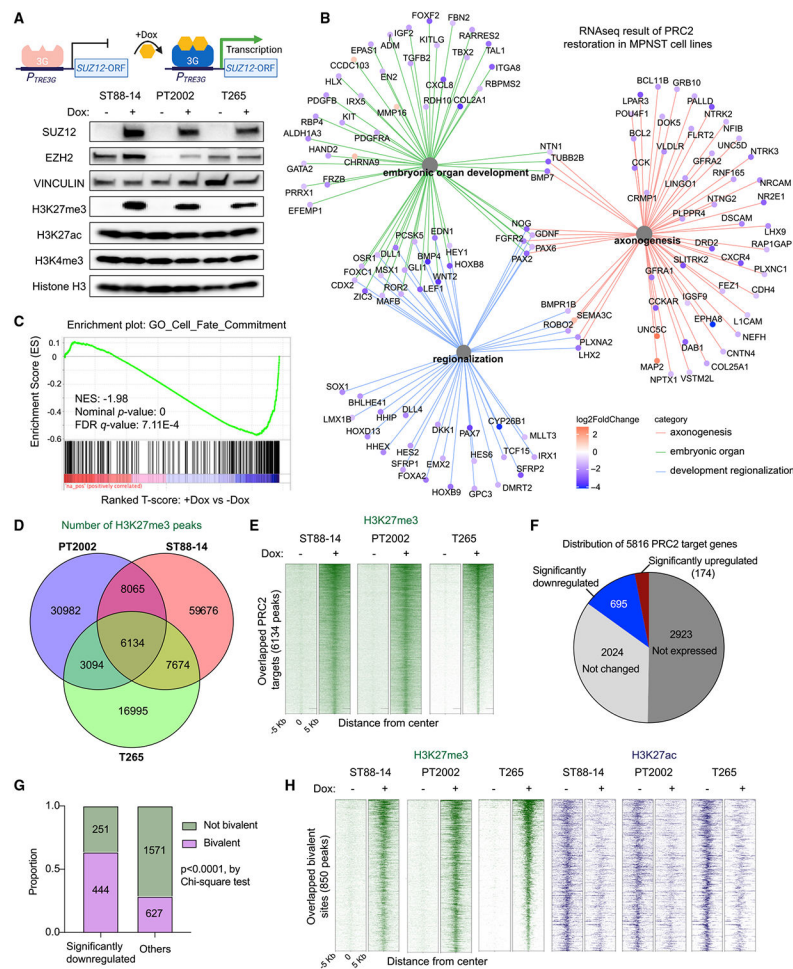- scRNA-seq reveals heterogeneity within the MPNST microenvironment

Figure 1. PRC2 restoration drives genome-wide gain of H3K27me3 occupancy

(A) Doxycycline (Dox)-induced reexpression of SUZ12 in MPNST cells restored trimethylated histone H3 lysine 27 (H3K27me3), as shown by western blotting.

(B) Network plot demonstrating the connection of three significantly enriched pathways of the differentially expressed genes (DEGs) caused by PRC2 restoration. DEGs were derived from a combined analysis of the RNA-seq results obtained from all three PRC2-null MPNST cell lines, comparing samples with induced expression of SUZ12 to controls; $p_{adj} < 0.05$, |log2 fold change| > 1.

(C) Gene set enrichment plot shows that PRC2 restoration significantly decreased genes in the "cell-fate commitment" pathway. NES, normalized enrichment score.

(D) Venn diagram showing the number of overlapped H3K27me3 peaks in three MPNST cell lines upon PRC2 restoration.

(E) PRC2 restoration drove the genome-wide gain of H3K27me3 occupancy as demonstrated by overlapped ChIP peaks in MPNST cells.

(F) Pie chart showing the distribution of transcriptional alterations among the 5,816 genes associated with H3K27me3 peaks found to be common in at least two cell lines upon Dox induction. Dark gray, genes not expressed; light gray, genes expressed but not changed; blue, significantly downregulated; red, significantly upregulated; $p_{adj} < 0.05$.

(G) Bar plot shows the enrichment of bivalent genes among the 695 downregulated genes upon PRC2 restoration.

(H) Heatmap of ChIP-seq signals shows that PRC2 restoration caused gain of H3K27me3 and loss of H3K27ac at 850 common bivalent sites in MPNST cells.
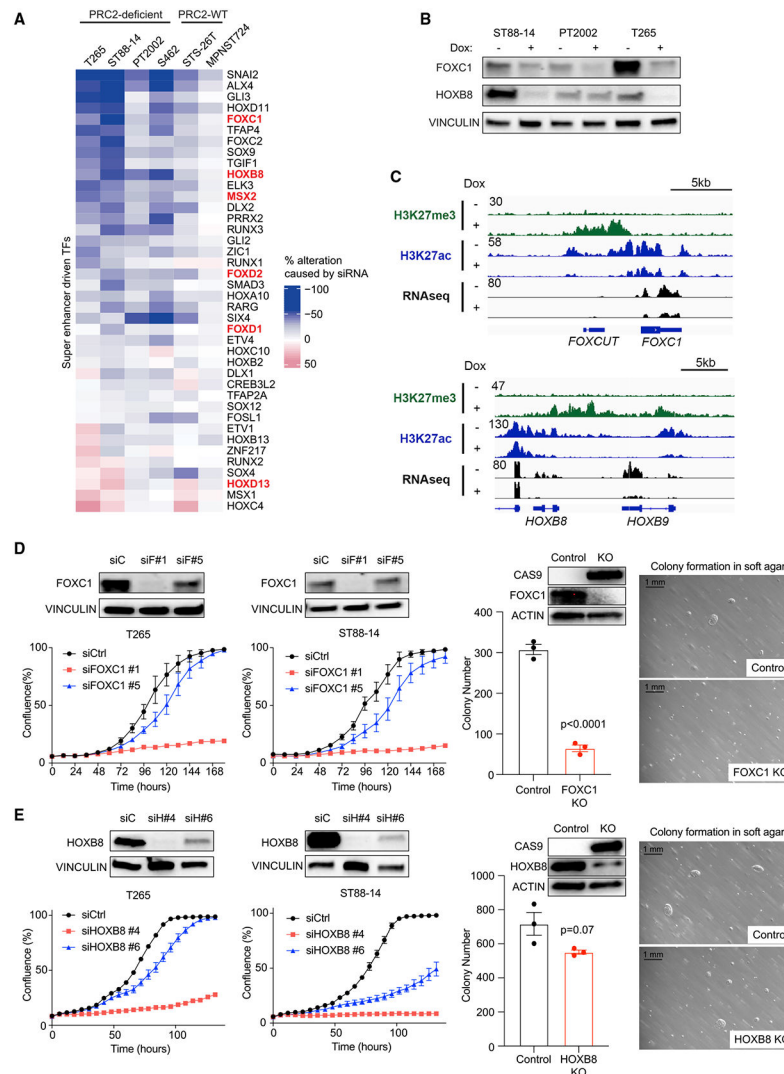
Figure 2. PRC2-regulated super-enhancer-driven transcription factors are essential to the survival of MPNST cells

(A) Heatmap showing the median percentage of reduction in proliferation when a candidate core TF was knocked down using three distinct siRNAs, in comparison with the control siRNA. Data are shown in the order of average median reduction from the highest to the lowest in four PRC2-deficient and two PRC2-WT cell lines. Data summarize two replicates per siRNA per cell line. Direct PRC2 targets are highlighted in red.

(B) Western blot shows the reduction of protein levels of FOXC1 and HOXB8 caused by Dox-induced SUZ12 reexpression.

(C) Example integrative genomics viewer (IGV) tracks around the *FOXC1* (top) and *HOXB8* (bottom) loci demonstrate the gain of H3K27me3, loss of super enhancer (SE), and transcriptional reduction accompanying the Dox-induced PRC2 restoration in T265 cells.

(D) Cell growth assay using individual siRNAs targeting FOXC1 in T265 (first panel) and ST88-14 (second panel). siC, siControl; siF#1, siFOXC1 #1; and siF#5, siFOXC1 #5. Quantification (third panel) and representative picture (fourth panel) of colony formation when FOXC1 was knocked out in T265 cells by CRISPR-Cas9 are shown.

(E) Cell growth assay using individual siRNAs targeting HOXB8 in T265 (first panel) and ST88-14 (second panel). siH#4, siHOXB8 #4, and siH#6, siHOXB8 #6. Quantification (third panel) and representative picture (fourth panel) of colony formation when HOXB8 was knocked out in T265 cells by CRISPR-Cas9 are shown. The average of five replicates is presented; mean ± SEM; scale bar, 1 mm.
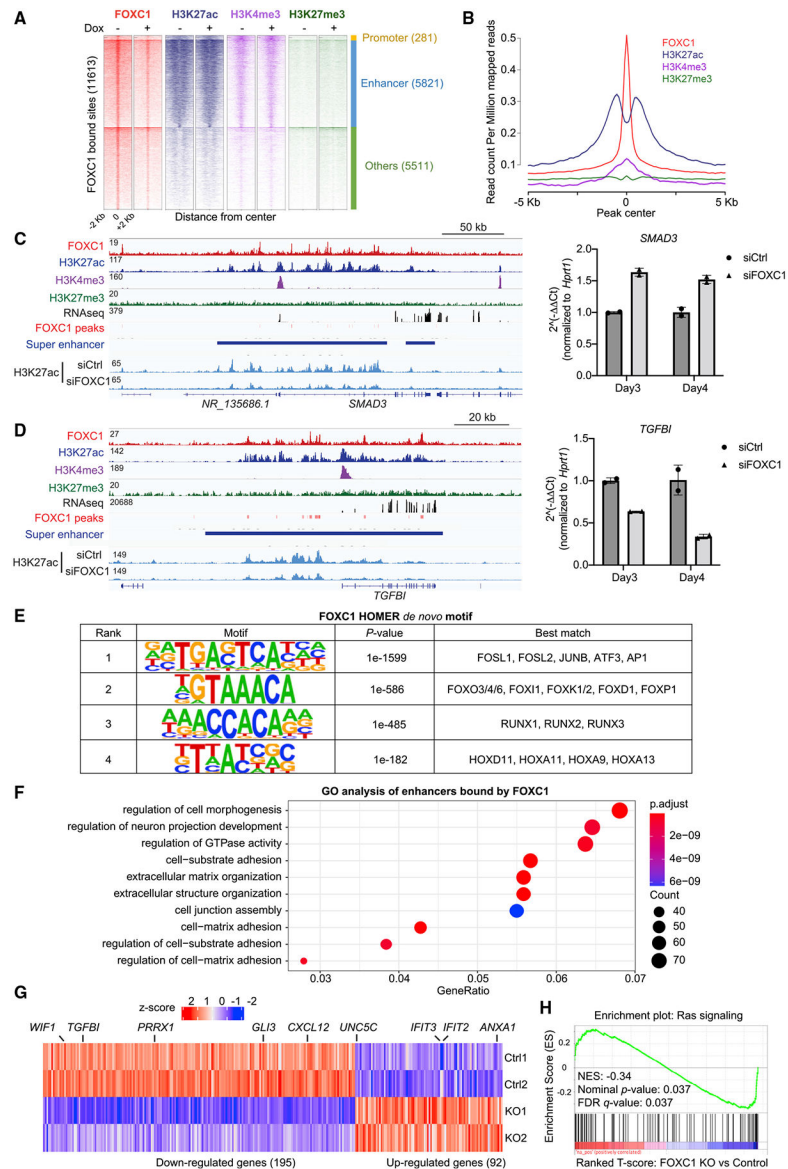
Figure 3. PRC2-regulated super-enhancer-driven FOXC1 determines the cell lineage specificity in MPNST cells

(A) Heatmap of ChIP-seq signal intensity of FOXC1, H3K27ac, H3K4me3, and H3K27me3 peaks in T265 without (−Dox) or with (+Dox) a functional PRC2 restored. ChIP-seq signals were calculated over 11,613 FOXC1 peaks that were segmented into three categories: promoter (281 peaks within 1,000 bp of the transcription start site), enhancer (5,821 peaks overlapping enhancers determined by ROSE using the H3K27ac ChIP-seq results), and others (5,511 peaks not at promoters or that do not overlap with enhancers).

(B) Composite plot of FOXC1, H3K27ac, H3K4me3, and H3K27me3 ChIP-seq signal intensity over 11,613 FOXC1 binding sites, showing that FOXC1 peaks overlapped with H3K27ac signals.

(C) IGV tracks of the *SMAD3* locus (left) and qRT-PCR quantification showing that *SMAD3* mRNA level (right) increased after FOXC1 knockdown.

(D) IGV tracks at the *TGFBI* locus (left), showing multiple FOXC1 peaks and the corresponding reduction of H3K27ac signals, as well as qRT-PCR quantification (right) of decreased expression of this gene.

(E) A table presenting the HOMER motif analysis results using FOXC1 ChIP-seq peaks. The top four *de novo* motif categories and the best-matched TFs representing that motif are shown.

(F) Gene ontology pathway analysis of genes associated with enhancers bound by FOXC1 in T265 cells.

(G) Heatmap showing the transcriptional alterations of direct FOXC1-targeted genes upon CRISPR-Cas9-mediated knockout of FOXC1 in T265 cells.

(H) Enrichment plot demonstrating that Ras signaling genes (De Raedt et al., 2014) were inhibited by FOXC1 knockout in T265 cells. NES, normalized enrichment score.
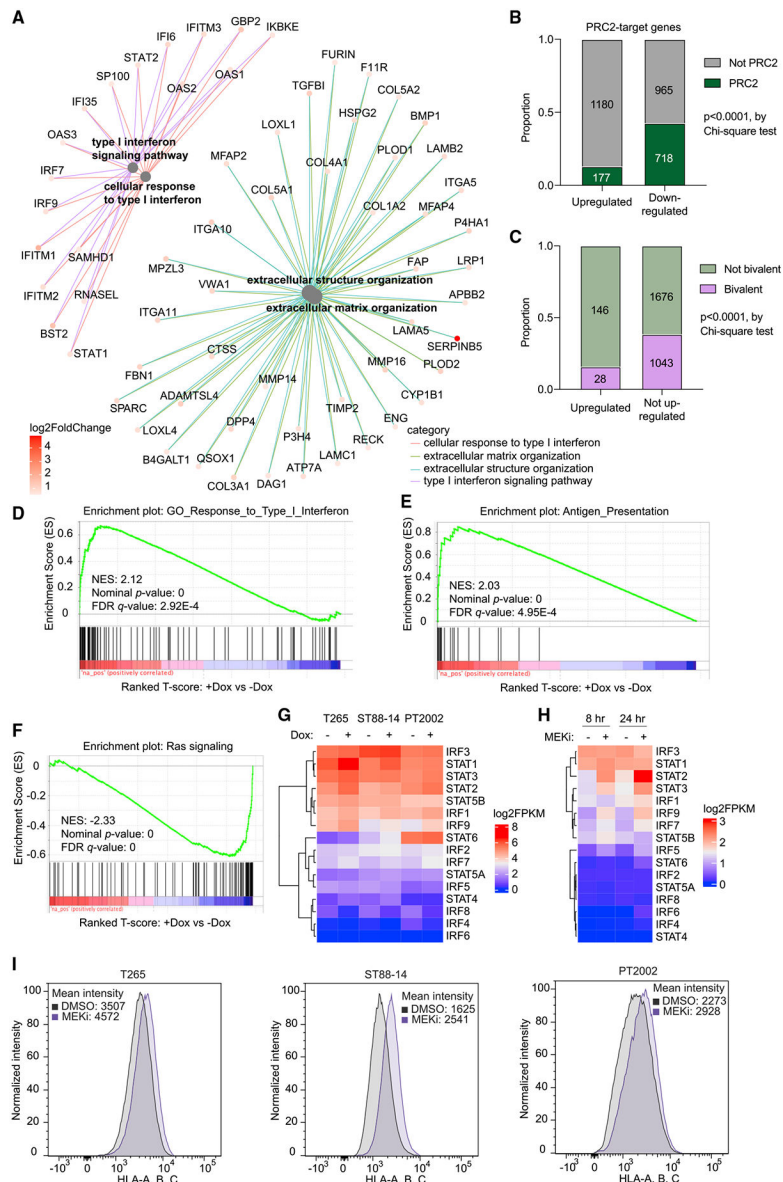
Figure 4. PRC2 restoration indirectly upregulates interferon signaling and antigen presentation

(A) Network plot showing the connections of upregulated genes upon PRC2 restoration (top four significantly enriched pathways shown). DEGs were derived from comparing the effect of PRC2 restoration to controls in all three PRC2-null MPNST cell lines using RNA-seq (Table S1).

(B) Quantification of DEGs demonstrating that the genes that were upregulated after PRC2 restoration were not direct PRC2 targets and did not gain H3K27me3 with a functional PRC2.

(C) Quantification of the PRC2-target DEGs shows that they were not bivalent genes.

(D) Enrichment plot demonstrating that PRC2 restoration significantly increased genes in the GO pathway "Response to type I interferon".

(E) Enrichment plot showing that genes associated with the pathway "Antigen presentation folder assembly and peptide loading of class I MHC" were significantly increased upon PRC2 restoration.

(F) Enrichment plot showing that Ras signaling genes (De Raedt et al., 2014) were inhibited by PRC2 restoration in T265 cells. NES, normalized enrichment score.

(G) Heatmap of key STAT and IRF transcription factors shows that mRNA expression levels of these transcription factors were increased by PRC2 restoration.

(H) Heatmap showing the transcriptional activation of STAT and IRF members caused by MEK inhibitor treatment in T265 cells.

(I) Histogram of flow cytometry result demonstrating the increase in cell-surface expression of MHCI in three PRC2-deficient cell lines after trametinib treatment.
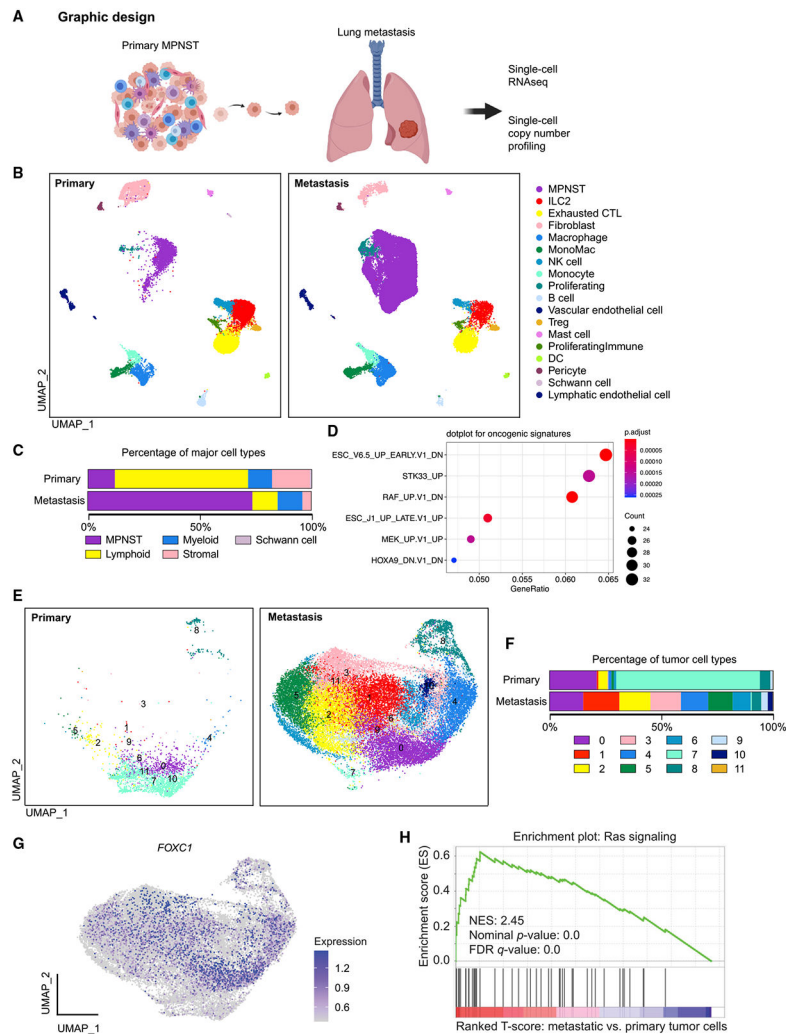
Figure 5. Single-cell sequencing reveals intratumoral heterogeneity of human malignant peripheral nerve sheath tumor

(A) Graphic illustration of the experimental approach for sampling the patient malignant peripheral nerve sheath tumors (MPNSTs).

(B) Uniform manifold approximation and projection for dimension reduction (UMAP) plot showing the distinct cell types detected in different stages of human MPNST using scRNA-seq.

(C) Bar graph demonstrating the percentage of major cell types detected in human MPNSTs (Table S4).

(D) Dot plot of the top six oncogenic pathways enriched among the marker genes of MPNST malignant cell.

(E) UMAP plot demonstrating the reclustering of malignant cells of human MPNST.

(F) Bar graph showing the quantification of the number of cells within each cluster of the reclustered malignant cells. Metastasized MPNST lost cluster 7 tumor cells.

(G) Feature plot of *FOXC1* expression in the primary and metastatic tumor cells.

(H) Gene set enrichment plot demonstrating that Ras signaling was enriched in the metastatic tumor cells.
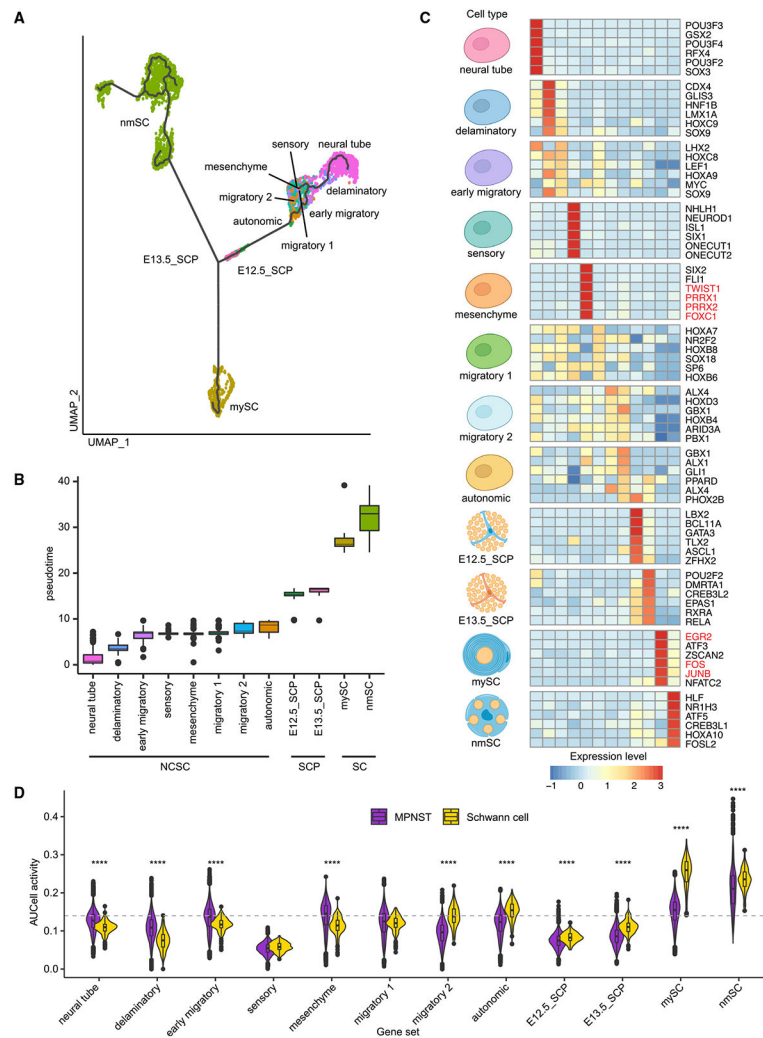
Figure 6. MPNST malignant cells demonstrate dedifferentiated phenotype regulated by PRC2

(A) UMAP plot of Schwann cell (SC) development from various cell types within the neural crest (NCSC) through SC precursors (SCP) to mature myelinating SC (mySC) and nonmyelinating SC (nmSC). Analysis was done using publicly available scRNA-seq data (see STAR Methods for details).

(B) Boxplot demonstrating the pseudotime of cells along the SC developmental trajectory.

(C) Transcriptional activity of SC development demonstrated by the most active transcription factors at each developmental stage.

(D) Comparison of AUCell activities of malignant MPNST cells with normal SCs using the marker genes of developing SCs (Table S5) at various developmental stages. Malignant cells demonstrated high activity of nmSC, mySC, and mesenchyme NCSC; ****p < 0.0001.
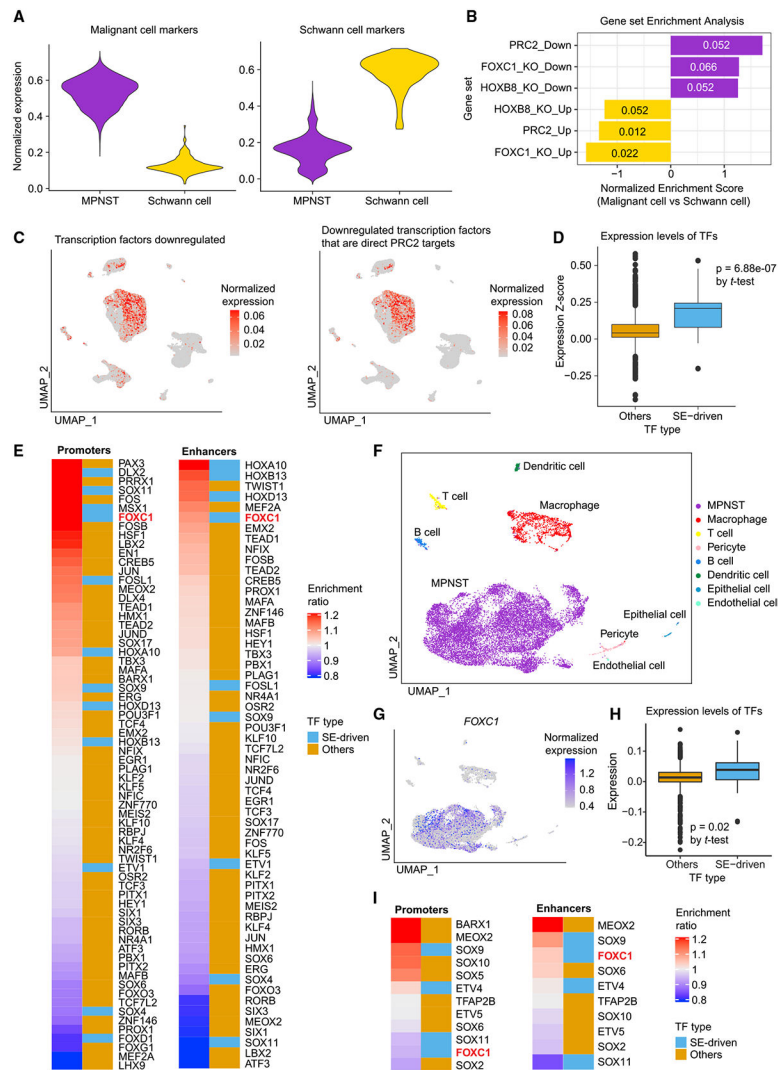
Figure 7. Activation of PRC2-regulated transcription factors drives the malignant program in human MPNST samples

(A) Violin plots of malignant cell marker genes (left) and Schwann cell (SC) marker genes (right) in the MPNST scRNA-seq dataset. Average expression of these marker genes in 27,796 malignant cells and 161 benign SCs is shown.

(B) Bar plot showing the results of pathway enrichment analysis among malignant cell and SC marker genes. Genes that were downregulated by HOXB8 or FOXC1 knockout or PRC2 restoration were significantly positively enriched among the malignant cell markers; p_{adj} is shown.

(C) UMAP plots demonstrating that the high expression of all PRC2-regulated TFs (left) and direct PRC2 targets among these TFs (right) was unique to the malignant MPNST cells.

(D) Boxplot of the expression levels of all TFs in malignant cells of human MPNST. TFs that had at least one assigned super enhancer (SE-driven) were expressed at a significantly higher level than the otherIs.

(E) Heatmaps of motif enrichment ratios of the TFs at the promoters (left) and in the enhancers (right) of marker genes of the MPNST malignant cells. The TFs are ranked from the highest to the lowest ratios. Blue, SE-driven TF; yellow, other TFs.

(F) UMAP plot of an MPNST single-cell dataset from another patient, featuring transcriptomic profiling of 14,967 cells.

(G) UMAP plot demonstrating that high expression levels of FOXC1 in the malignant cells (12,721 cells) could distinctly separate them from the tumor microenvironment.

(H) Boxplot of expression levels of all TFs in malignant cells of the second human MPNST. TFs that had at least one assigned super enhancer (SE-driven) were expressed at a significantly higher level compared with the other TFs.

(I) Heatmap of motif enrichment ratios of the TFs at the promoters (left) and in the enhancers (right) of marker genes of the second MPNST's malignant cells, ranked from the highest to the lowest ratio. Blue, SE-driven TF; yellow, other TFs.

KEY RESOURCES TABLE

REAGENT or RESOURCE	SOURCE	IDENTIFIER
Antibodies		
FOXC1	Cell Signaling Technology	Cat# 8758S; RRID: AB_2797657
FOXC1	Invitrogen	Cat# PA1-807; RRID: AB_2247078
EZH2	Cell Signaling Technology	Cat# 5246S; RRID: AB_10694683
SUZ12	Cell Signaling Technology	Cat# 3737S; RRID: AB_2196850
EED	Abcam	Cat# ab4469; RRID: AB_2262066
H3K27me3	Cell Signaling Technology	Cat# 9733S; RRID: AB_2616029
H3K27me3	Millipore	Cat# 07-449; RRID: AB_310624
H3K4me3	Cell Signaling Technology	Cat# 9751S; RRID: AB_2616028
H3K27ac	Abcam	Cat# ab4729; RRID: AB_2118291
pERK	Cell Signaling Technology	Cat# 9101S; RRID: AB_331646
ERK	Cell Signaling Technology	Cat# 9102S; RRID: AB_330744
IgG isotype control	Cell Signaling Technology	Cat# 3900S; RRID: AB_1550038
VINCULIN	Cell Signaling Technology	Cat# 13901S; RRID: AB_2728768
B-ACTIN	Cell Signaling Technology	Cat# 3700S; RRID: AB_2242334
CAS9	Cell Signaling Technology	Cat# 14697S; RRID: AB_2750916
IgG HRP conjugated secondary	Cell Signaling Technology	Cat# 7076; RRID: AB_330924
IgG HRP conjugated secondary	Cell Signaling Technology	Cat# 7074; RRID: AB_2099233
HOXB8	Santa Cruz	Cat# sc-517156
PRRX2	Invitrogen	Cat# PA5-37195; RRID: AB_2553954
IgG HRP light chain specific secondary	Jackson Laboratory	Cat# 221-002-171
HLA-A,B,C	Biolegend	Cat# 311406; RRID: AB_314875
IgG2a, K Isotype Ctrl	Biolegend	Cat# 400214; RRID: AB_2800438
BST2	Cell Signaling Technology	Cat# 19277S; RRID: AB_2798815
B2M	Cell Signaling Technology	Cat# 12851S
IFITM1	Cell Signaling Technology	Cat# 13126S; RRID: AB_2798126
IFITM2	Cell Signaling Technology	Cat# 13530S; RRID: AB_2798248
IFITM3	Cell Signaling Technology	Cat# 59212S; RRID: AB_2799561
Stat1-6	Cell Signaling Technology	Cat# 93130T
Bacterial and virus strains		
Edit-R Inducible Lentiviral Cas9	Dharmacon	Cat# VCAS11227
Chemicals, peptides, and recombinant proteins		
DMEM Medium	Thermo Fisher	Cat# 11995081
Fetal Bovine Serum	Bio-techne	Cat# S11550
Penicillin-Streptomycin	Thermo Fisher	Cat# 15070063
RPMI Medium	Thermo Fisher	Cat# 11879020
Puromycin	Thermo Fisher	Cat# A1113803
Doxycycline	Sigma Aldrich	Cat# D9891
10x Cell Lysis Buffer	Cell Signaling Technology	Cat# 9803
Protease Inhibitor Cocktail	Thermo Fisher	Cat# 78430

REAGENT or RESOURCE	SOURCE	IDENTIFIER
4x LDS Sample Loading Buffer	Invitrogen	Cat# NP0008
Skim Milk Powder	MP Biomedicals	Cat# 902887
SuperSignal West Pico Chemiluminescent substrate	Thermo Fisher	Cat# 34080
SuperSignal West Femto Chemiluminescent substrate	Thermo Fisher	Cat# 34094
Clarity Max Western ECL Substrate	Bio-Rad	Cat# 1705062
Tween Ultrapure	Affymetrix	CAS# 9005-64-5
Tris Buffered Saline, 10X	Corning	REF# 46-012-CM
Lipofectamine RNAiMAX	Invitrogen	Cat# 13778-150
SPRIselect reagent	Beckman	Cat# B23317
Opti-MEM	Gibco™	Cat# 31985062
CellTiter 96 AQueous One Solution	Promega	Cat# G3582
Blasticidin	Invitrogen	Cat# A1113902
Puromycin	Invitrogen	Cat# A1113802
Anti-Fc receptor	Biolegend	Cat# 422301
Fixable Viability Dye eFluor™ 506	Invitrogen	Cat# 65-0866-14
collagenase I	STEMCELL Technologies	Cat# 07416
dispase II	MilliporeSigma	Cat# D4693-1G
DNase I	Invitrogen	Cat# 18047019
AO/PI viability dye	Nexcelom	Cat# CS2-0106-5ML
Critical commercial assays		
Essen IncuCyte FLR	Essen BioScience	Cat# 4515
Bradford Assay Dye	Bio-Rad	Cat# 5000006
Total Histone Extraction Kit	Epigentek	OP-0006-100
Dynabeads M-280 Sheep anti-Rabbit IgG Magnetic Beads	Invitrogen	Cat# 11203D
RNeasy Mini Kit	Qiagen	Cat# 74004
TruSeq Stranded Library Preparation Kit	Illumina	Cat# 20020594
ChIP-IT High Sensitivity kit	Active Motif	Cat# 53040
TruSeq ChIP Library Prep Kit	Illumina	Cat# IP-202-1012
Zymo DNA Clean and Concentrator-5 Kit	Zymo Research	Cat# D4014
NexteraDNA Library Prep kit	Illumina	Cat# FC-131-1024
High-Capacity RNA-to-cDNA kit	ThermoFisher	Cat# 4387406
CUT&RUN assay kit	Cell Signaling Technology	Cat# 86652
SimpleChIP ChIP-seq DNA library Prep Kit	Cell Signaling Technology	Cat# 56795
Multiplex Oligos for Illumina® (Dual Index Primers)	Cell Signaling Technology	Cat# 47538
Deposited data		
Next generation sequencing data generated for this study	This study	GSE183309
ATAC-seq data generated	This study	GSE183305
ChIP-seq data generated	This study	GSE183306
RNAseq data generated	This study	GSE183307
Single-cell RNAseq data generated	This study	GSE183308
CUT&RUN data generated	This study	GSE202671

REAGENT or RESOURCE	SOURCE	IDENTIFIER
E9.5 neural crest cell single-cell sequencing data	Soldatov et al. (2019)	GSE129114
E12.5/E13.5 adrenal medulla cell single-cell sequencing data	Furlan et al. (2017)	GSE150150
Mature Schwann cell single-cell sequencing data	Wolbert et al. (2020)	GSE142541
Experimental models: Cell lines		
T265 cell line	Laboratory of Dr. Karlyne Reilly	RRID: CVCL_S805
S462 cell line	Laboratory of Dr. Karlyne Reilly	RRID: CVCL_1Y70
SNF96.2 cell line	Laboratory of Dr. Karlyne Reilly	RRID: CVCL_K281
SNF02.2 cell line	ATCC	Cat# CRL-2885; RRID: CVCL_K280
STS-26T cell line	Laboratory of Dr. Steven Porcelli	RRID: CVCL_8917
MPNST724 cell line	Laboratory of Dr. Nancy Ratner	RRID: CVCL_AU20
ST88-14 cell line	Laboratory of Dr. Nancy Ratner	RRID: CVCL_8916
PT2002 cell line	Johns Hopkins NF1 Biospecimen Repository	N/A
PT2031 cell line	Johns Hopkins NF1 Biospecimen Repository	N/A
PDX cell line	Laboratory of Dr. Rosandra Kaplan	N/A
HEK293 cells	Takara Bio	Cat# 632180
Oligonucleotides		
Negative control siRNA	Qiagen	Cat# 1027281
siFOXC1-1	Qiagen	Cat# SI00026138
siFOXC1-5	Qiagen	Cat# SI03037713
siHOXB8-4	Qiagen	Cat# SI00440685
siHOXB8-6	Qiagen	Cat# SI04311916
Recombinant DNA		
ORF of human SUZ12	GenScript	Cat# NM_015355
PLVX-TetOne-Puro vector	Takara Bio	Cat# 631849
pLentiGuide-Puro vector	GenScript	
Software and algorithms		
Quantity One Software	Bio-Rad	https://www.bio-rad.com/en-us/product/quantity-one-1-d-analysis-software
BWA	Li and Durbin, 2009	https://github.com/lh3/bwa
DESeq2	Love et al., 2014	https://bioconductor.org/packages/release/bioc/html/DESeq2.html
macs2 v2.2.6	Zhang et al., 2008	https://github.com/macs3-project/MACS
DeepTools	Ramírez et al., 2016	https://deeptools.readthedocs.io/en/develop/
IGV genome browser	Robinson et al., 2011	https://software.broadinstitute.org/software/igv/
STAR	Dobin et al., 2013	https://github.com/alexdobin/STAR
RSEM	Li and Dewey, 2011	https://github.com/deweylab/RSEM
R package ComplexHeatmap	Gu et al., 2016	https://bioconductor.org/packages/release/bioc/html/ComplexHeatmap.html

REAGENT or RESOURCE	SOURCE	IDENTIFIER
BEDOPS	Neph et al., 2012	https://bedops.readthedocs.io/en/latest/
Trimmomatic	Bolger et al., 2014	http://www.usadellab.org/cms/?page=trimmomatic
BEDTools	https://bedtools.readthedocs.io/en/latest/	https://bedtools.readthedocs.io/en/latest/index.html
HOMER	Heinz et al., 2010	http://homer.ucsd.edu/homer/download.html
Rank Ordering of Super-Enhancer (ROSE)	Loven et al., 2013	https://bitbucket.org/young_computation/rose
FlowJo software	BD	https://www.flowjo.com/solutions/flowjo/downloads
Loupe scDNA Browser	10X Genomics	https://support.10xgenomics.com/single-cell-dna/software/downloads/latest
Euler algorithm in TFBSTools	Tan and Lenhard, 2016	https://bioconductor.org/packages/release/bioc/html/TFBSTools.html
NGSplot	Shen et al., 2014	https://github.com/shenlab-sinai/ngsplot
Cell Ranger	10X Genomics	https://support.10xgenomics.com/single-cell-gene-expression/software/downloads/latest
Seurat v4.0	Butler et al., 2018; Stuart et al., 2019	https://satijalab.org/seurat/
inferCNV	inferCNV of the Trinity CTAT Project	https://github.com/broadinstitute/inferCNV
ReactomePA	Yu and He, 2016	https://bioconductor.org/packages/release/bioc/html/ReactomePA.html
GraphPad Prism	GraphPad	N/A
Biorender	Biorender	https://biorender.com
HOCOMOCO v11	Kulakovskiy et al., 2016	https://hocomoco11.autosome.org
JASPER 2020	Fornes et al., 2020	https://jaspar.genereg.net
SCENIC	Aibar et al., 2017	https://scenic.aertslab.org
Monocle3	Cao et al., 2019; Trapnell et al., 2014	https://cole-trapnell-lab.github.io/monocle3/
Other		
In-Fusion HD	Takara Bio	Cat# 639643
SpectraMax M3 microplate reader	Molecular Devices	Cat# 89429-536
Trans-Blot Turbo Transfer system	Bio-Rad	N/A
ChemiDoc	Bio-Rad	N/A
Agilent 2100 Bioanalyzer	Agilent	N/A
HiSeq4000 sequencer	Illunima	N/A
EpiShear Probe Sonicator	Active Motif	N/A
Thermomixer	Eppendorf	N/A
Illumina NextSeq machine	Illumina	N/A
Incucyte S3 live cell analysis system	Essen BioScience	N/A
Nikon Eclipse TE300 microscope	Nikon	N/A
LSRFortessa	BD	N/A
GentleMACS dissociator	Miltenyl Biotec	N/A

REAGENT or RESOURCE	SOURCE	IDENTIFIER
Cellometer Auto 2000	Nexcelom	N/A
Chromium Controller	10x Genomics	N/A